



Analyses of robotic traverses and sample sites in the Schrödinger basin for the HERACLES human-assisted sample return mission concept

DOI:

[10.1016/j.asr.2016.05.041](https://doi.org/10.1016/j.asr.2016.05.041)

Document Version

Accepted author manuscript

[Link to publication record in Manchester Research Explorer](#)

Citation for published version (APA):

Steenstra, E. S., Martin, D. J.P., McDonald, F. E., Paisarnsombat, S., Venturino, C., O'Hara, S., Calzada-Diaz, A., Bottoms, S., Leader, M. K., & Klaus, K. K. (2016). Analyses of robotic traverses and sample sites in the Schrödinger basin for the HERACLES human-assisted sample return mission concept. *Advances in Space Research*. <https://doi.org/10.1016/j.asr.2016.05.041>

Published in:

Advances in Space Research

Citing this paper

Please note that where the full-text provided on Manchester Research Explorer is the Author Accepted Manuscript or Proof version this may differ from the final Published version. If citing, it is advised that you check and use the publisher's definitive version.

General rights

Copyright and moral rights for the publications made accessible in the Research Explorer are retained by the authors and/or other copyright owners and it is a condition of accessing publications that users recognise and abide by the legal requirements associated with these rights.

Takedown policy

If you believe that this document breaches copyright please refer to the University of Manchester's Takedown Procedures [<http://man.ac.uk/04Y6Bo>] or contact uml.scholarlycommunications@manchester.ac.uk providing relevant details, so we can investigate your claim.



1 Analyses of Robotic Traverses and Sample Sites in the 2 Schrödinger basin for the HERACLES Human-Assisted 3 Sample Return Mission Concept

4 Edgar S. Steenstra^a, Dayl J. P. Martin^b, Francesca E. McDonald^b, Sarinya Paisarnsombat^c
5 Christian Venturino^d, Sean O'Hara^e, Abigail Calzada-Diaz^f, Shelby Bottoms^g, Mark K. Leader^g,
6 Kurt K. Klaus^g, Wim van Westrenen^a, Debra H. Needham^h, David A. Kringⁱ

7 ^a*Faculty of Earth and Life Sciences, VU University, Amsterdam, The Netherlands*

8 ^b*School of Earth, Atmospheric and Environmental Sciences, University of Manchester, UK*

9 ^c*Department of Earth Sciences, University of New Brunswick, Canada*

10 ^d*Department of Geology, University at Buffalo, Buffalo, USA*

11 ^e*Department of Earth and Environmental Science, University of Illinois at Chicago, Chicago, USA*

12 ^f*Department of Earth and Planetary Science, Birkbeck University of London, UK*

13 ^g*The Boeing Company, Houston, USA*

14 ^h*Goddard Space Flight Center, Oak Ridge Associated Universities, USA*

15 ⁱ*Center for Lunar Science and Exploration, Lunar and Planetary Institute, USA*

16

17 *Corresponding author: email address: e.s.steenstra@vu.nl

18 Telephone: +316–29573045

19

20 Abstract

21

22 Near-future exploration of the Moon will likely be conducted with human-operated robotic assets.
23 Previous studies have identified the Schrödinger basin, situated on the far side of the Moon, as a prime
24 target for lunar science and exploration where a significant number of the scientific concepts reviewed
25 by the National Research Council (NRC, 2007) can be addressed. In this study, two robotic mission
26 traverses within Schrödinger basin are proposed based on a 3 year mission plan in support of the
27 HERACLES human-assisted sample return mission concept. A comprehensive set of modern remote
28 sensing data (LROC imagery, LOLA topography, M³ and Clementine spectral data) has been
29 integrated to provide high-resolution coverage of the traverses and to facilitate identification of

30 specific sample localities. We also present a preliminary Concept of Operations (ConOps) study based on
31 a set of notional rover capabilities and instrumental payload. An extended robotic mission to
32 Schrödinger basin will allow for significant sample return opportunities from multiple distinct geologic
33 terrains and will address multiple high-priority NRC (2007) scientific objectives. Both traverses will offer
34 the first opportunity to (i) sample pyroclastic material from the lunar farside, (ii) sample Schrödinger
35 impact melt and test the lunar cataclysm hypothesis, (iii) sample deep crustal lithologies in an uplifted
36 peak ring and test the lunar magma ocean hypothesis and (iv) explore the top of an impact melt sheet,
37 enhancing our ability to interpret Apollo samples. The shorter traverse will provide the first opportunity
38 to sample farside mare deposits, whereas the longer traverse has significant potential to collect SPA
39 impact melt, which can be used to constrain the basin-forming epoch.

40

41 **Keywords:** Schrödinger, Moon, Exploration, Lunar, Sample Return Mission

42

43 **1. Introduction**

44 The international community agrees (e.g., NRC, 2007; Crawford et al., 2012) that exploration of the
45 Moon can address fundamentally important scientific questions, while providing a credible path for
46 human exploration into the Solar System. The International Space Exploration Coordination Group
47 (ISECG), an interagency organization developing an integrated Global Exploration Roadmap (GER), is
48 currently exploring a human-assisted robotic sample return mission concept (HERACLES; Human-
49 Enhanced Robotic Architecture and Capability for Lunar Exploration and Science). This mission concept
50 involves a series of landings that would expand access to the lunar surface. The first landing would
51 deploy the rover. Two additional landings of a reusable ascent vehicle at other sites along the traverse
52 would deploy a suite of experimental packages. The rover collects samples and performs in-situ analyses
53 during each section of the traverse for a number of months, and rendezvous with the ascent vehicle to
54 transfer the collected samples. A crew in the Orion capsule or an exploration Deep Space Habitat (eDSH)
55 could tele-operate the rover while orbiting at the Earth-Moon L2 Lagrange point above the farside of the
56 Moon (Burns et al., 2013; Pratt et al., 2014). The samples for each section would then be transferred
57 from the ascent vehicle to the eDSH, which would transfer the samples to the Orion crew vehicle for
58 return to Earth.

59 One of the most comprehensive studies of lunar science objectives conducted by the US National
60 Research Council produced a report that outlined eight scientific concepts and thirty-five prioritized
61 investigations (NRC, 2007). A large number of studies were then conducted to determine the locations

62 on the lunar surface where those investigations could be addressed (Kring and Durda, 2012). This work
63 showed that the Schrödinger basin, situated within the South Pole-Aitken (SPA) basin, is the best
64 location on the Moon for addressing the highest priority and largest number of objectives.

65 For example, a robotic sample return mission to Schrödinger basin would test the cataclysm
66 hypothesis (NRC Goal 1), would provide insights into the the petrologic structure of the lunar interior
67 (NRC Goals 2 and 3), would assess the thermal and compositional evolution of the Moon (NRC Goals 3
68 and 5), would provide insights into basin forming processes (NRC Goal 6) and would investigate regolith
69 processes and surface weathering (NRC Goal 7). A recent study of Kumar et al. (2015) suggests that the
70 Schrödinger basin is also an interesting locality for studying local seismic events and could be tied into a
71 tetrahedral seismic array for global lunar coverage (Tian et al., 2013). In addition, several targets within
72 the peak ring structure are likely to receive no or little illumination year-round and are therefore
73 believed to be targets suitable for in-situ resource utilization (ISRU) (Kring et al., 2014; NRC Goal 4). The
74 pyroclastic vent is believed to be a prominent source of volatiles and, therefore, also has a significant
75 ISRU potential (Kring, 2014). Previous studies have referenced these benefits to justify a range of sites
76 and traverses that are located within the Schrödinger basin. However, these mission designs involved
77 either human exploration on the lunar surface (Bunte et al., 2011; O'Sullivan et al., 2011) or a robotic
78 exploration mission that does not exceed more than one lunar day (Potts et al., 2015).

79 In this study, two possible traverses for long-term (~3 year) robotic exploration in the Schrödinger
80 basin are investigated by integrating a wide range of remote sensing datasets that include topography,
81 compositional spectra, and high-resolution imagery (Martin et al., 2016; McDonald et al., 2016). The
82 proposed traverses are based on previously identified key targets within Schrödinger basin (O'Sullivan et
83 al., 2011; Potts et al., 2015; Hurwitz and Kring, 2015) and are designed to address the key science and
84 exploration objectives that are prevalent throughout the international lunar science community (NRC,
85 2007; Crawford et al., 2012).

86

87 **2. The Schrödinger basin**

88 The Schrödinger impact basin (Fig. 1, 2) is located on the lunar farside (-75°, 132.5°) and is the second-
89 youngest basin formed during the basin-forming epoch. It is situated within the South Pole-Aitken (SPA)
90 basin, the oldest and largest impact basin on the Moon. Schrödinger measures ~320 km in diameter and
91 its basin floor has a minimum elevation of ~4.5 km below the crater rim. Despite subsequent
92 modification by both volcanism and secondary cratering from nearby large impacts, Schrödinger is
93 remarkably well preserved. It features a distinctive inner peak ring measuring ~150 km in

94 diameter, extending up to ~2.5 km above the basin floor, and possessing a discontinuous
95 southern region due, probably, to overlapping with the Amundsen-Ganswindt basin (Shoemaker et al.,
96 1994). The peak ring preserves pre-Schrödinger materials uplifted from a depth of ~20-30 km, implying
97 the presence of mid- to deep-crustal lithologies (Kring et al., 2013). The modification of Schrödinger
98 basin is likely to have exposed SPA-derived material within its southern wall which would be of great
99 significance as sampling this material would address the two top ranking NRC (2007) science objectives
100 (Hurwitz and Kring, 2015).

101

102

Fig. 1, Fig. 2

103

104 **3. Methods**

105 Traverse routes within the Schrödinger basin were constructed in ArcGIS© 10.1 using Lunar
106 Reconnaissance Orbiter Camera (LROC) NAC (Narrow Angle Camera; 0.5 m/pix resolution) and WAC
107 (Wide Angle Camera; 100 m/pix) images, integrated with a Digital Elevation Map (DEM from Lunar
108 Orbiter Laser Altimeter). Spectral reflectance data, collected by M³ and documented in the geologic map
109 of Kramer et al. (2013), was also used to supplement these datasets to select sample sites along
110 traverses. The WAC images were combined with Lunar Orbiter Laser Altimeter (LOLA) data to create a
111 DEM with a spatial resolution of 100 m/pix. A set of 3D images were created by combining NAC imagery
112 and the DEM in ArcScene©. Spectral data from the Clementine mission were used to interpret the FeO
113 variability across the basin (Lucey et al., 2000; Kramer et al., 2013; Hurwitz and Kring, 2015).

114

115 **4. Rover capabilities and operations**

116 *4.1 Rover capabilities and notional instrument payload*

117 The interpretation of returned samples benefits significantly from knowledge of the geological
118 context of the sampled area. A first order criterion for instrument selection is, therefore, their
119 demonstrated capability to provide regional and lateral geological context of the sample site. A
120 notional payload that might be used to perform in-situ analyses along the proposed traverse include a
121 Ground Penetrating Radar (GPR) (ExoMars WISDOM, Shearer et al., 2010), a HD imager (Mars Science
122 Laboratory MastCam, Shearer et al., 2010), a Gamma Ray Spectrometer or GRS (JH APL, Wieczorek et
123 al., 2015) and a Microscope Imager (MI) (Mars Exploration Rover, Arvidson and May, 2010). Other
124 instruments may include an arm-mounted Alpha Particle X-Ray Spectrometer or APXS (Mars
125 Exploration Rover, Arvidson and May, 2010) and a Neutron Spectrometer or NS (Lunar Prospector /

126 Hydra, Shearer et al., 2010).

127 A continuously operating GPR would provide a measure of the lateral and vertical distribution
128 of subsurface lithologies along the traverses and a HD camera would be used to image different areas
129 along the traverse to provide regional geological context. A MI can be used to investigate the physical
130 and chemical properties either of the target material at the sub-millimeter scales, or adjacent
131 material to provide additional geological context. Subsurface (<10 cm) elemental abundances for a
132 wide range of elements can be obtained using a GRS in conjunction with an arm-mounted APXS. The
133 APXS is particularly important as it can provide rapid compositional analysis (~30-60 minutes) of the
134 target material with a reasonable degree of accuracy (Rieder et al., 2003). Operation of a NS would
135 assess volatile composition and distribution and, therefore, provide a measure of ISRU potential
136 within the Schrödinger basin. To sample regolith or other poorly consolidated material, a percussive
137 scoop or shovel tool would be required (Craft et al., 2009; Zacny et al., 2009). Collection of uniformly
138 sized lithic fragments would require a rake tool, which may have to be developed.

139 Sampling of boulders and outcrops along the traverse also requires the robotic asset to remove
140 these samples without completely destroying textural data. Techniques that could be implemented
141 include coring devices (Johnson et al., 2009; Myrick et al., 2012; Paulsen et al., 2012; Zacny et al.,
142 2012, 2013) or rock chipping devices (Barnouin-Jha et al., 2004). Prior to identification and analysis
143 procedures, a Rock Abrasion Tool (RAT) could be used to expose the interior of lunar rock samples
144 (Myrick et al., 2004).

145 Technical aspects of the assumed notional instrument payload, including weight and average
146 power consumption, are summarized in Table 1. The proposed traverses in this study could be
147 explored with any instrument payload and the notional payload included here is simply used to
148 demonstrate the science potential of the traverses and to create a rational concept of operations
149 from which to determine analytical timelines and data bandwidths. The rover speed is assumed to be
150 0.36 km/hr based on the expected speed of the Resource Prospector rover (Loftin et al., 2013), a
151 conservative estimate given the speed of 0.8-2 km/hr of the Soviet Lunokhod rover (Seeni et al.,
152 2010). We consider a maximum traversable slope of 16°, because wheel enabled systems show
153 considerable difficulties at higher slopes due to a sudden drop in slip ratio (Seeni et al., 2010; Potts et
154 al., 2015).

155

156

Table 1

157

158

159

4.2 Concept of Operations (ConOps)

160

161

162

163

164

165

166

167

168

169

170

171

172

173

174

175

176

177

178

179

180

181

182

183

184

185

Table 2

186

4.3 Soil mechanics and rover trafficability

187

188

189

The operations that the rover will perform at stations as well as start-up and packing down processes required for traversing along the lunar surface are defined as the ConOps. The HERACLES human-assisted sample return mission concept is based on a 3 year mission duration and the rover must therefore be able to survive a large number of lunar nights (~14 Earth days) during which it will hibernate. This strategy is similar to the Lunokhod 1 rover that survived for 7 to 11 lunar nights and Lunokhod 2 that survived ~5 lunar nights (Petrov, 1972; NASA Space Science Data Center, 1970, 1973). The time estimated to deploy the rover is ~20 hours (Potts et al., 2015). Before and after each hibernation period, ~24 hours is allocated for powering down and up of the rover (Potts et al., 2015). During lunar days (~14 Earth days), we assume constant rover operation which would require that teams in Orion and on Earth dually conduct rover operations. Each of the three sample transfer procedures from the rover to the ascent vehicle are estimated to take ~10 hours (Potts et al., 2015).

Along the traverse, sampling and in-situ analysis stations were identified. At each sampling station, the rover will first stop to collect a GigaPan panorama using the surface imaging camera (~8 hrs). The rover will then select a target and will move to its location, where it will position itself (~0.5 hrs). Once in place, the rover is expected to conduct a number of analyses, including APXS (~3.5 hrs/analysis), GRS (~1.5 hrs/analysis) and MI (~1.5 hrs/analysis). The GPR is expected to operate constantly while traversing, but NS analyses would only be used at specific targets (~6.5 hrs/analysis). Images taken before and after sampling will provide context for the returned samples (~1 hr). An additional ~4 hours is required for sample collection (~3 hrs) and storage (~1 hr). Assuming one APXS, MI and GRS analysis, ~19.5 hours would be spent at each sampling station (Table 2). For in-situ analysis stations, the average time spent at each station is estimated to ~15.5 hours. This does not take into account any additional time that may be required to repeat analyses, load commands, or to address unforeseeable issues (e.g., obstacle avoidance or stuck wheels). There is, however, plenty of margin in the ConOps schedule to mitigate these types of issues as described below.

Lunar soil properties may affect the maneuverability and power usage of a robotic rover and is an important constraint on possible traverse designs. Photographic observations of footprints and Lunar Roving Vehicle (LRV tracks) from the Apollo era allow for the calculation of surficial porosity, cohesion,

190 and friction angles of lunar regolith (Mitchell et al., 1972). These results suggest that the rims of
191 primary and secondary craters covered with significant amounts of ejecta should be circumvented
192 due to their low trafficability. For example, the Lunokhod 2 rover experienced significant wheel
193 sinkage (~20 cm) when it traversed the soft soils within the rim of a Mare Serenitatis crater (Carrier et
194 al., 1991). The wall slump material within Schrödinger basin may be analogous to the soft soils
195 encountered on Apollo 15, during which the LRV rover wheels sank ~13 cm into the lunar regolith
196 (Carrier et al., 1991). However, the weight of the rover is likely to be significantly lower than the LRV
197 and its much lower speed would reduce wheel spin, which would reduce the risk of significant wheel
198 sinkage. A particular area of interest is the pyroclastic unit within Schrödinger, because the physical
199 properties of lunar pyroclastic soils are poorly constrained. Apollo 17 regolith core samples from the
200 Shorty crater rim suggested that the orange glass deposit was unusually compact, exhibiting high
201 cohesion (Mitchell et al., 1973). The bearing capacity of a lunar soil is defined as its capability to
202 support applied loads and is therefore a proxy for possible trafficability of a lunar rover. Using the
203 surficial properties obtained for the upper part of the latter drill core combined with observed
204 boulder tracks within the pyroclastic deposits close and within the vent (the Appendix), the bearing
205 capacity of the pyroclastic material can be calculated using Terzaghi's bearing capacity equation for
206 circular footings (Terzaghi, 1948) (Eq. 1):

$$207$$
$$208 \quad Q = 1.3 N_c C + \rho g N_q D_f + 0.6 \rho g N_\gamma R_f \quad (1)$$
$$209$$

210 where N_c , N_q , and N_γ are dimensionless numbers for soil shear conditions based on the internal friction
211 angle. The boulder and associated track dimensions were used for the depth of footing (D_f) and radius
212 of footing (R_f) values (Fig. 2). Cohesion (C) value is taken to be 10^3 dynes/cm² (Moore, 1970; Hovland
213 and Mitchell, 1969; Mitchell et al., 1973), gravity (g) as 163 cm/s² and the boulders are assumed to be
214 spherical. Assuming an internal friction angle of 30° and estimated pyroclastic soil density of 2.0 g/cm³
215 (Moore, 1970; Hovland and Mitchell, 1969; Mitchell et al., 1973), we calculate a bearing capacity (Q) of
216 3.46×10^6 dynes/cm², comparable to the 9.28×10^5 dynes/cm² calculated by Moore (1970) for general
217 lunar surface capacities (the Appendix). The friction angle of lunar pyroclastic deposits is not known.
218 However, an increase of the friction angle to 35° , the suggested value for the upper 15 cm of regolith
219 (Houston et al., 1972; Hovland and Mitchell, 1969; Mitchell et al., 1972, 1973), results in an increase of
220 the bearing capacity to 6.41×10^6 dynes/cm². The higher value associated with Schrödinger's
221 pyroclastic unit demonstrates that it has a higher cohesion and capacity for added mass, meaning the

222 trafficability for a robotic rover is likely sufficient (Venturino et al., 2016). This is important, as ~15%
223 and ~30% of the proposed short and long traverses are located within the pyroclastic deposits.
224 However, there is some uncertainty in these calculations. For example, the reported internal friction
225 angles derived from boulder tracks range considerably between previous studies (10-50°; Moore, 1970;
226 Mitchell et al., 1973). It is also not clear to what extent the Apollo 17 orange glass soil density is
227 representative of the pyroclastic material within Schrödinger. Our calculations also do not take the
228 effect of the local slope on Terzaghi's bearing capacity equation for circular footings into account. If
229 HERACLES is pursued, then this issue will need to be examined further.

230

231 *4.4 Sample mass considerations*

232 For the traverses proposed in this study, we assume an arbitrary sample mass of 10 kg per landing.
233 However, the sample mass that can be returned will depend on the payload capability of the ascent
234 vehicle. Assessment of the payload capability of a possible ascent vehicle suggests it is likely that >10
235 kg of sample mass can be accommodated (the Appendix). Another constraint on returned sample
236 mass is the storage capability of the considered sample containers that are required for sample
237 transfer between the ascent vehicle and the eDSH.

238 Calculations assuming a prototype spherical sample container (Pratt et al., 2014) suggests total
239 sample masses can exceed 30 kg (the Appendix). The assumed 30 kg of total sample mass is,
240 therefore, a baseline. A greater mass of representative returned samples would significantly increase
241 the productivity of a robotic exploration mission in Schrödinger basin. These additional samples could
242 be collected from a wide range of identified in-situ stations along both traverses. The size of sample
243 collected at each station in the concept study is dependent on the type of lithology involved and is
244 based on recommendations from the Curation and Analysis Planning Team for Extraterrestrial
245 Materials (CAPTEM) (Shearer et al., 2007).

246

247 **5. Sampling key units within Schrödinger basin**

248 A significant number of key lithological units are present within the Schrödinger basin and sampling
249 these units will address a wide range of scientific goals defined by the NRC (2007). These units include
250 SPA-derived material and Schrödinger impact melt, crustal lithologies, secondary impactor material,
251 and volcanic deposits (pyroclastic and mare) (Fig. 1, 2). Hurwitz and Kring (2015) showed that the
252 southern basin wall of Schrödinger basin is a promising target for sampling SPA-derived material. In
253 conjunction with samples of Schrödinger impact melt sheet, samples of SPA-derived material can be

254 used to anchor the early Earth-Moon impact flux and basin forming epoch, addressing the top two
255 science objectives (NRC, 2007). Along the peak ring area, a significant section of the lunar crust is
256 exposed and includes anorthositic, noritic, and troctolitic lithologies (Fig. 1, 2). Sampling these
257 lithologies would test models of planetary differentiation and crustal evolution (NRC Goals 2 and 3),
258 provide ground-truth standards for remote sensing applications, and yield important insights into the
259 dynamical processes that occur during peak-ring basin forming events (NRC Goal 6). A large number
260 of secondary craters thought to be related to the formation of Antoniadi crater and Orientale basin
261 (Fig. 1, 2) have also been identified within the Schrödinger basin. By targeting such secondary craters,
262 exotic material from different regions of the Moon could be sampled and analyzed (NRC Goal 1).
263 Samples of the mare and pyroclastic volcanic deposits within the Schrödinger basin (Fig 1, 2) provide
264 insight into their mantle source depths, the delivery mechanism to the surface (NRC Goals 2 and 3),
265 and lunar thermal evolution (NRC Goal 5). The pyroclastic deposits may also be volatile-rich and
266 sampling this material would evaluate its ISRU potential. Regolith samples and in-situ analyses will
267 provide insights into regolith processes and surface weathering on the lunar surface (NRC Goal 7).

268

269 **6. Traverses**

270 Two traverses were designed within an ESA-specified total traverse distance of 100 to 300 km. The first
271 traverse is ~207 km long and is designed to explore the basin interior. The second, longer traverse is
272 ~291 km long and is designed to explore the region between the basin interior and basin wall.

273

274 *6.1 The short traverse*

275 The short traverse is situated within the inner peak ring area of the Schrödinger basin. Sampling
276 along this traverse would access 6 of the geologic units defined by Kramer et al. (2013) and has the
277 potential to address a significant number of the NRC (2007) science priorities (Table 2, Fig. 4, 5). The
278 traverse is ~207 km long and accommodates 50 stations with 18 sampling stations (the Appendix).
279 The other 32 stations are identified as in-situ analysis stations, that are expected to significantly
280 contribute to the geological context and, therefore, understanding of the returned samples. The
281 traverse has been divided into three sections with three landing sites. The first section is based on
282 Potts et al. (2015), but with a proposed 3 km shift to the north-west for the first landing site. This shift
283 is required to prevent any contamination of the ascent vehicle activities on the first sample station
284 (Immer et al., 2011). Stations S1-S9 will be visited in the first section and stations S10-S33 and S34-S50
285 will be investigated in the second and third leg of the traverse, respectively (the Appendix).

286 Sampling stations S1, S14 and S24 are located within the pyroclastic deposits unit (*Ep*) that is
287 associated with a pyroclastic vent (Wilhelms et al., 1979; Shoemaker et al., 1994; Gaddis et al., 2003;
288 Kramer et al., 2013). The deposits are morphologically distinct from the surrounding terrain and their
289 M^3 spectral heterogeneities suggest the deposits are more FeO-rich than the surrounding basin floor
290 (Kramer et al., 2013). This type of volcanic material was emplaced by a volatile-driven fire fountain
291 eruption (Rutherford and Papale, 2009; Wetzel et al., 2015; Fig. 6). This is based on the analyses of
292 presumably similar lunar pyroclastic deposits (e.g., Apollo 17 orange glass) which show a surface
293 coating that is enriched in highly volatile elements relative to the bulk silicate Moon (Meyer et al.,
294 1975). This is thought to be the result of deposition of volatile-rich vapors onto the glass beads during
295 cooling of the volcanic gas clouds that envelop the beads (Hauri et al., 2015; Fig. 6). Previous studies
296 have suggested the pyroclastic volcanism within Schrödinger basin occurred <2 Ga ago, which is
297 relatively recent (Shoemaker et al., 1994) compared with the inferred age range of ~4.0-1.2 Ga of
298 mare magmatism on the Moon (Hiesinger et al., 2011). Stations S1, S14 and S14 will provide the first
299 opportunity to sample pyroclastic material in geological context from the lunar farside. Absolute
300 dating of these samples will yield an absolute chronology of relatively young lunar processes and,
301 therefore, will additionally constrain the lunar thermal evolution (NRC Goal 5). Samples of this
302 material would also provide insights into the compositional evolution of the lunar interior (NRC Goals
303 2, 3, and 5) by determination of their source depth, formation mechanism, and ISRU potential (Kring,
304 2014; Kring et al., 2014). The results from in-situ analyses at stations S9-S13 and S15-S26 will provide
305 insights into the vertical and lateral variability of the pyroclastic deposits, and can be used to further
306 constrain its compositional variability and distribution (NRC Goal 2, 3 and 5).

307
308 Fig. 4, 5
309

310 After station S1, the traverse continues along the pre-Nectarian peak ring (*pNpr*), where stations S2,
311 S3 and S5 will sample lithologically distinct boulders derived from the peak ring (Fig. 5a, b). Spectral
312 observations from the Kaguya spacecraft and the M^3 instrument indicate the presence of anorthositic,
313 noritic, and troctolitic lithologies at the peak ring (Kramer et al., 2013) (Fig. 1). This suggests that the
314 peak ring material is composed of pre-Nectarian deep crust, and possibly upper mantle material,
315 uplifted during the basin forming event (Kramer et al., 2013; Fig. 2). The anorthositic unit is interpreted
316 to be crystalline material that has not been significantly shocked or melted, representative of pre-impact
317 crustal material. This is derived from (1) the unmistakable spectral signature of pure anorthosite and (2)

318 the estimated exhumation depth of the peak ring that exceeds the thickness of cumulative ejecta from
319 all observable ancient basins in proximity to Schrödinger basin (Kramer et al., 2013). The troctolitic unit
320 is likely to reflect lower crustal material or potentially entrained upper mantle material and may provide
321 information of the pre-uplift depth, estimated to be 20-30 km (Kring et al., 2013). The eastern part of
322 the peak ring is well covered by M³ spectral reflectance data and is in close proximity to the pyroclastic
323 vent, providing an opportunity for maximizing the science and exploration potential in a relatively small
324 area (Bunte et al., 2011; O'Sullivan et al., 2011; Potts et al., 2015). The identification of boulders and
325 associated trails allows for sampling of peak material at slopes accessible to conventional rover designs
326 (Potts et al., 2015) and will yield the first in-context samples of pristine middle and lower lunar crustal
327 lithologies.

328 This will test models of planetary differentiation and crustal evolution, therefore addressing the
329 majority of the science priorities within NRC (2007) Goals 2 and 3. It will also yield insights into the
330 dynamical processes that occur during peak ring basin forming events (NRC Goal 6) and provide ground-
331 truth standards to test and refine interpretations based on remote sensing spectral data. In-situ analysis
332 station S4 on pre-Nectarian peak ring material will provide additional insights into the vertical and
333 lateral diversity of primitive, lunar crust. Because the competing models for peak ring formation (cf.
334 Grieve and Cintala 1998 and Kring et al., 2013
335 <http://www.hou.usra.edu/meetings/lpsc2016/pdf/1659.pdf>) assume different strengths for the material
336 in peak rings, it will be important to produce high-resolution images of any peak-ring outcrops and
337 boulders from those outcrops along the traverse.

338 Station S6 will involve the collection of a rake sample and is located close to the fracture north of
339 the peak ring, where detailed imaging of the cliff wall will provide a regional geological cross section (Fig.
340 5b, c). In-situ analysis at station S7 and sampling at station S8 will study impact melt breccias from the
341 inter-peak ring floor material (*lipr*) unit, which is thought to contain peak ring material and Schrödinger
342 impact melt (Shoemaker et al., 1994; Kramer et al., 2013). This would be the first opportunity to explore
343 and sample the top of an impact melt sheet on the Moon. Compositional spectra (M³) suggest the
344 dominant composition of the upper portion of the melt sheet is noritic (Kramer et al., 2013). This may
345 imply that the Schrödinger melt sheet differentiated during cooling, which is a topic of ongoing debate
346 (e.g., Vaughan et al., 2013). Samples of the excavated floor material within Schrödinger basin could
347 therefore be used to determine to what extent the melt sheet has differentiated (NRC Goal 6) and
348 would greatly enhance our ability to interpret Apollo samples. The S6 samples would also provide the

349 age of the Schrödinger impact event and, therefore, constrain the end of the basin-forming epoch (NRC
350 Goal 1).

351 A number of in-situ analysis stations (S27-S30, S34-S36, S41-S44, S48-S50) and sampling stations
352 (S32, S37, S38, S45-S49) are situated within the inner-peak ring smooth floor material (*Isip*), where the
353 rover will sample and analyze additional Schrödinger melt sheet material. This will provide insights into
354 the vertical and lateral variability of the Schrödinger melt sheet (NRC Goal 6).

355 The rover then continues to stations S31 and S33 where it will sample a relatively smooth and
356 spectrally FeO-rich unit, previously identified as mare basalt deposits (*Em*) (Shoemaker et al., 1994;
357 Kramer et al., 2013). At stations S39 and S40, the rover will use in-situ analyses to further study the
358 mare deposits. It is also likely that at stations S34, S37, S38, S41- S43, presumably inner-peak ring
359 smooth floor material (*Isip*), additional mare material can be sampled and/or analyzed. The lateral
360 distribution of the latter sampling and in-situ analysis stations allows for studying melt sheet processes
361 and the lateral compositional and structural variability of the melt sheet (NRC Goal 6). They will also
362 further constrain the compositional variability of the mare deposits (NRC Goal 2, 3 and 5). The first in-
363 context mare basalt samples from the farside will provide insights into the nearside-farside dichotomy
364 of the lunar surface and could test vital aspects of the lunar magma ocean (LMO) hypothesis, including
365 cumulate overturn and the lateral and vertical extent of the LMO. They will also provide insight into
366 their mantle source depths and delivery mechanism to the surface (NRC Goals 2, 3 and 5).

367

368

Fig. 6, 7

369

370 At stations S45-47 the rover will obtain three rake samples near two large secondary craters that
371 have been identified to originate from Antoniadi crater and Orientale basin (Shoemaker et al., 1994;
372 Kramer et al., 2013) (Fig. 1b, 2). The physics of ballistic sedimentation suggest that secondary ejecta
373 deposits mostly consist of reworked target material (Oberbeck et al., 1975). In order to assess the
374 likelihood of sampling exotic material within the secondary craters identified along the traverse, the
375 model of Morrison and Oberbeck (1978) was used to calculate the diameter and velocity of ejecta
376 fragments that created the secondary craters in Schrödinger basin, assuming a 45 degree launch angle.
377 For a secondary crater of a given diameter, the ratio of surviving primary material to reworked target
378 material within the ejecta deposit was calculated (Fig. 7). The size-velocity distribution indicates that the
379 fragments that formed the largest secondary craters in Schrödinger were kilometer-scale blocks moving
380 at approximately 0.8-2 km/s. At these velocities, it is expected that approximately 5-18% of primary

381 Antoniadi material would survive, whereas <5% of primary Orientale material would have survived (Fig.
382 7). Sampling this material has the potential to provide highland material, derived from the Orientale
383 basin, and possibly SPA material, derived from Antoniadi crater (O’Sullivan et al., 2011) (NRC Goal 1).

384 The traverse then continues along a sinuous rill that is likely associated with the mare volcanism
385 within Schrödinger (Kramer et al., 2013) and a high FeO bluff thought be of volcanic origin (Shoemaker
386 et al., 1994). Sampling at stations S48 and S49, and in-situ analysis at station S50, will provide insights
387 into the nature of these features and can be used to determine the compositional and lateral variability
388 of volcanic deposits within Schrödinger basin (NRC Goal 2, 3 and 5).

389 At a significant number of stations along both traverses, the rover will sample and/or analyze
390 regolith. These results can be used to address three of the four scientific objectives within NRC (2007)
391 Goal 7. The majority of primary craters along the short traverse are of Eratosthenian or Copernican age
392 based on qualitative assessment of crater degradation (Trask, 1971; the Appendix). These craters could
393 be sampled to more precisely determine the lunar impact flux through time (NRC Goal 1).

394 The estimated total collected sample mass from the short traverse is ~28.5 kg and will address 21
395 individual investigations identified by NRC (2007), corresponding to 68% of the remaining objectives. If
396 the experimental package deployed from the second and/or third ascent vehicle landing includes a
397 seismometer, the lunar interior structure and crater formation processes could also be explored (NRC
398 Goal 1 and 6). Sampling and in-situ stations for the short traverse are summarized the Appendix.

399 The short traverse can be completed in ~3.5 months, assuming the rover is continuously operated
400 during lunar days with a constant rover speed of 0.36 km/hr during traversing and without repeated
401 analyses at sampling or in-situ stations (Table 2). If the number of in-situ analyses at each station is
402 extended to three analyses per type of in-situ analysis it would take the rover ~6 months to complete
403 the traverse. This would correspond to a 90% and 83% time margin on the total 3 year mission duration.
404 If the landings and ascents were scheduled on a fixed 12 month cadence, the traverse can be completed
405 in ~25 months, providing a 30% margin on schedule. Three in-situ analyses per type of in-situ analysis at
406 each station would increase the total traverse time to ~26.5 months, corresponding to a 27% margin.

407

408 *6.2 Long traverse*

409 The long traverse encompasses both the inner- and outer-peak ring zone of Schrödinger basin and
410 also traverses 6 geological terrains (Fig. 8, 9). It measures ~291 km in length and includes 66 stations
411 (including the stations near the southern basin wall proposed by Hurwitz and Kring, 2015). Samples

412 would be collected at 16 of these stations. The other stations are in-situ analysis stations that are
413 required to provide sufficient geological context for the returned samples (the Appendix).

414 Stations S1-S14 and landing site 1 of the long traverse are identical to the short traverse and will,
415 thus, sample the three spectrally distinct crustal lithologies from the peak ring (S2, S3, S5), Schrödinger
416 melt sheet material (S8) and pyroclastic material (S1, S14). In-situ analyses will be performed on peak
417 ring lithologies (stations S4, S6) and pyroclastic material (stations S9-S13, L1-L2) and will help to
418 constrain the lateral variability of pristine lunar crustal material and pyroclastic material.

419 In the south the traverse crosses inner-peak ring smooth floor material (*isip*), a zone of secondary
420 crater fields associated with Orientale basin (*isc*) and smooth outer-peak ring floor material (*isop*)
421 (Kramer et al., 2013). The rover will perform in-situ analyses on smooth inner-peak ring floor material at
422 stations L6-L8 and will characterize the existence and lateral extent of melt sheet differentiation (NRC
423 Goal 6). Sampling stations L12A/L12B, L25 and L30 are located within the secondary crater field and
424 provide the opportunity to sample surviving exotic material from Antoniadi crater and/or Orientale
425 basin (Kramer et al., 2013; Fig. 7). Additional in-situ analyses will be performed (Stations L3-L5, L9-L15,
426 L21-L25, L26-32, L37-L38) along the traverse to additionally constrain the occurrence and composition of
427 exotic material within Schrödinger basin. The lateral and vertical distribution of stations along this area
428 is suitable for determining the extent of lateral and vertical mixing of local and ejecta material (NRC Goal
429 6). In-situ analyses at these stations can also be used to constrain the composition of the underlying
430 smooth outer-peak ring floor material (*isop*), providing insights into the lateral and compositional
431 variability of Schrödinger melt sheet and, therefore, in melt sheet processes (NRC Goal 6). Samples from
432 stations L12A/L12B, L25 and L30 will also provide an absolute age of the Schrödinger impact event (NRC
433 Goal 1).

434 Sampling stations L16 and L19 are located near the wall slump in the south-eastern part of the peak
435 ring. Coverage of M³ data suggests the presence of olivine-bearing, pyroxene-bearing and anorthositic
436 lithologies. Sampling at these stations combined with in-situ analyses (Stations L17, L18 and L20) will
437 provide additional insights into the lateral and vertical variability of the lunar crust within the
438 Schrödinger basin (NRC Goals 2 and 3).

439 In the third section of the long traverse, the rover will have an opportunity to study the smooth
440 hummocky floor material unit (*ish*) (Stations L33-L41, L50, L51) identified as the most Mg-rich norite
441 floor unit within Schrödinger (Kramer et al., 2013). This will provide insights into the compositional
442 range of the Schrödinger melt sheet and the occurrence and/or extent of melt sheet differentiation
443 (NRC Goal 6).

444 Close to the final landing site, there will be an opportunity to sample material from the southern
445 wall (*lw*) (stations L45, L46, L47 as suggested by Hurwitz and Kring (2015), or alternatively, stations L43,
446 L44, L46 and L48 based on this study). A recent study of Hurwitz and Kring (2015) suggest the FeO-rich
447 signature that is thought to represent an SPA impact melt component in Schrödinger wall outcrops and
448 floor material extends from the eastern to the south-eastern wall of Schrödinger basin, with estimates
449 up to 6-8% of SPA material. Compositional M^3 spectra of low-Ca pyroxene in the southern basin wall has
450 been interpreted to indicate the material has a noritic composition (Kramer et al., 2013).

451 Sampling SPA material would provide an age of the SPA basin-forming event and, therefore, would
452 anchor the early Earth-Moon impact flux (NRC Goal 1). The results from in-situ analysis stations L38-L42
453 and L49 will be used to additionally constrain the composition of SPA material and to provide geological
454 context of the returned samples. Analyses of regolith along the base of the southern wall could also
455 shed light on the physical properties of ancient regolith (NRC Goal 7).

456 Crater degradation states of >10m craters along the traverse suggest the majority are of
457 Eratosthenian and Copernican age using the qualitative descriptions of Trask (1971) (the Appendix).
458 Samples of this material can be used to additionally constrain the lunar impact flux through time. The
459 long traverse would collect a total sample mass of 29.5 kg (the Appendix) and can address a significant
460 amount (65%) of the remaining individual investigations identified in the NRC (2007) report.

461 Using the ConOps from Table 2 it is expected that the traverse can be completed within ~5.5
462 months, which allows for one GRS, APXS and MI analysis and one panorama view at each station.
463 Repeating the latter analyses three times at each station would extend total traverse time to ~7 months,
464 providing 85% and 80% margin on both traverse times relative to a 3 year mission duration. If the
465 landings and ascents were scheduled on a fixed 12 month cadence, the traverse can be completed in
466 ~26 months, providing 28% margin. The total traverse time is increased to ~27 months if each analysis is
467 repeated 3 times, corresponding to a 25% margin on the total 3 year mission duration.

468

469

Fig. 8, 9

470

471 **7. Future work**

472 Future studies should include a solar irradiance study of Schrödinger basin to aid with determining
473 optimal mission start dates and to further constrain the times necessary to complete each traverse. This
474 would be especially important along the south-eastern portion of the peak ring. When rover
475 specifications have been confirmed, the rover capabilities (e.g., speed, need to hibernate, and

476 communication data rates) and instrumentation payload should be reassessed. The effect of these
477 changes on ConOps times should then be taken into account to further evaluate traverse times.

478 Several bench craters have been identified along the traverse, which would aid in estimation of
479 the regolith thickness along the traverses. A TiO₂ map would be useful to investigate the nature of the
480 pyroclastic and mare deposits in more detail. The traverses proposed in this study have unique subset
481 routes and, therefore, address different objectives and the possibility of combining both traverses
482 should be assessed given the time margin for completing the latter traverses.

483

484 **8. Conclusions**

485 It has been shown that a long duration, human-assisted robotic mission to the Schrödinger basin can
486 address all 7 of the remaining lunar science concepts as determined by the NRC (2007). Two robotic
487 traverses with sample return capabilities within Schrödinger basin have been constructed for a 3 year
488 mission duration within the HERACLES mission architecture (Landgraf et al., 2015). Both the short- (~207
489 km) and long (~291 km) traverse accomplish many of the same objectives, but subsets of each traverse
490 are also unique and, therefore, will address different scientific objectives. The trafficability of the
491 Schrödinger pyroclastic deposits was assessed and suggests the vent could be explored for ISRU
492 potential. The proposed traverses would address the majority (>61-65%) of the individual investigations
493 identified in the NRC (2007) report. Notional ConOps suggests the short and long traverse can be
494 completed within ~3 and ~5.5 months , providing a ~91% and ~85% margin relative to a 3 year mission
495 duration. If the landings and ascents were scheduled on a fixed 12 month cadence, the short and long
496 traverses are expected to be completed within ~24.5 and ~26 months, giving a margin of ~32% and
497 ~28%. The selected sample stations and notional ConOps suggest both traverses are highly attractive for
498 long-term robotic exploration of the lunar surface from both a scientific and exploration science point of
499 view.

500

501 **Acknowledgements**

502 This work was carried out through the 2015 Lunar Exploration Summer Intern Program hosted by the
503 Lunar and Planetary Institute (LPI). This research was supported in part by NASA Solar System
504 Exploration Research Virtual Institute contract NNA14AB07A (David A. Kring PI). We thank the staff at
505 LPI for their help and support throughout the internship. LPI Contribution No. ###.

506

507 **References**

508 Arvidson, R.E., May, L. Planetary Science Decadal Survey Mars 2018 MAX-C Caching Rover. NASA mission
509 concept study, 2010.

510 Barnouin-Jha, O.S., Barnouin-Jha, K., Cheng, A.F., Willey, C., Sadilek, A. Sampling a Planetary Surface with
511 a Pyrotechnic Rock Chipper. IEEE Aerospace Conference Proceedings. Paper 1102, 2004.

512 Bunte, M.K., Porter, S., Robinson, M.S. A sortie mission to Schrödinger Basin as reconnaissance for
513 future exploration. In: Garry, W. B., Bleacher, J. E. (Eds.), *Analogs for Planetary Exploration*. The
514 Geological Society of America Special Paper 483. Boulder, CO, pp. 533-546, 2011.

515 Burns, J.O., Kring, D.A., Hopkins, J.B., Norris, S., Lazio, T.J. W., Kasper, J. A lunar L2-Farside exploration
516 and science mission concept with the Orion multi-purpose crew vehicle and a teleoperated
517 lander/rover. *Adv. Space. Res.* 52, 306-320, 2013.

518 Carrier, W.D. III, Olhoeft, G.R., Mendell, W. Physical Properties of the Lunar Surface. In: *Lunar*
519 *Sourcebook*, G.H. Heiken, D.T. Vaniman, and B.M. French (eds.), Cambridge University Press,
520 Cambridge, 1991.

521 Cintala, M. J., Grievem R. A. F. Scaling impact melting and crater dimensions: Implications for the lunar
522 cratering record. *Meteorit. Planet. Sci.* 33, 889-912, 1998.

523 Craft, J., Wilson, J., Chu, P., Zacny, K., Davis, K. Percussive digging systems for planetary research. In: IEEE
524 Aerospace Conf., Big Sky MT, 2010.

525 Crawford, I.A., Anand, M., Cockell, C.S., Falcke, H., Green, D.A., Jaumann, R., Wieczorek, M.A. Back to the
526 Moon: the scientific rationale for resuming lunar surface exploration. *Planet. Space. Sci.* 74, 3-14,
527 2012.

528 Delano, J. Chemistry and liquidus phase relations of Apollo 15 red glass: Implications for the deep lunar
529 interior. *Proc. Lunar Planet. Sci. Conf.* 11th, pp. 251-288, 1980.

530 Gaddis, L.R., Staid, M.I., Tyburczy, J.A., Hawke, B.R., Petro, N.E. Compositional analyses of lunar
531 pyroclastic deposits. *Icarus* 161, 262-280, 2003.

532 Green, D. H., Ringwood, A. E. Significance of a primitive lunar basaltic composition present in Apollo 15
533 soils and breccias. *Earth Planet. Sci. Lett.* 19, 1-8, 1973.

534 Hauri, E.H., Saal, A.E., Rutherford, M.J., Van Orman, J.A. Water in the Moon's interior: Truth and
535 consequences. *Earth Planet. Sci. Lett.* 252-264, 2015.

536 Hiesinger, H., Head, J., Wolf, U., Jaumann, R., Neukum, G. Age and stratigraphy of lunar mare basalts: A
537 synthesis. *Spec. Pap. Geol. Soc. Am.* 477, 1-51, 2011.

538 Houston, W.N., Hovland, H.J., Mitchell, J.K. Lunar Soil Porosity and Its Variation as Estimated from
539 Footprints and Boulder Tracks. Proc. 3rd Lunar Sci. Conf., vol. 3, MIT Press (Cambridge, Mass.), pp.
540 3255-3263, 1972.

541 Hovland, H.J., Mitchell, J.K. Friction angle of lunar surface soils estimated from boulder tracks: Space
542 Sciences Laboratory, Lunar Surface Engineering Properties Experiment Definition, Second Quarterly
543 Report, Univ. of California, 117 p, 1969.

544 Hurwitz, D.M., Kring, D.A. Potential sample sites for South Pole-Aitken basin impact melt within the
545 Schrödinger basin. Earth Planet. Sci. Lett. 427, 31-36, 2015.

546 Immer, C., Lane, J., Metzger, P., Clements, S. Apollo video photogrammetry estimation of plume
547 impingement effects. Icarus 214, 46-52, 2011.

548 Johnson, J.B., Mungas, G.S., Zacny, K., Albert, D.G., Banerdt, B., Buehler, M., Elphic, R.C., Lambert, J.,
549 Sturm, M., Johnson, K. Lunar and Planetary Science Conference XL. Abstract 1987, 2009.

550 Kramer, G.Y., Kring, D.A., Nahm, A.L., Pieters, C.M. Spectral and photogeologic mapping of Schrödinger
551 Basin and implications for post-South Pole-Aitken impact deep subsurface stratigraphy. Icarus 223,
552 131-148, 2013.

553 Kring, D.A., Durda, D. D. A Global Lunar Landing Site Study to Provide the Scientific Context for
554 Exploration of the Moon. LPI Contribution No. 1694, Lunar and Planetary Institute, Houston, TX,
555 688p, 2012.

556 Kring, D.A., Kramer, G.Y., Potter, R.W.K. Interpreting the depth of origin of the Schrödinger peak ring and
557 implications for other impact basins. Large Meteorite Impacts and Planetary Evolution V. Abstract
558 3069, 2013.

559 Kring, D. A., Kramer, G. Y., Potter, R. W. K. Interpreting the depth of origin of the Schrödinger peak ring
560 and implications for other impact basins. Large Meteorite Impacts and Planetary Evolution V.
561 Abstract 3069, 2013.

562 Kring, D.A. Production of volatiles at lunar pyroclastic volcanic vents. In: Annual Meeting of the Lunar
563 Exploration Analysis Group. Abstract 3056, 2014.

564 Kring, D.A., Kramer, G.Y., Bussey, D.B., Hurley, D.M. Prominent volcanic source of volatiles in the South
565 Polar Region of the Moon. In: Annual Meeting of the Lunar Exploration Analysis Group. Abstract
566 3057, 2014.

567 Kumar, P. S., Sruthi, U., Krishna, N., Lakshmi, K. J. P., Menon, R., Amitabh, B., Krishna, G., Kring, D. A.,
568 Head, J. W., Goswami, J. N., Kiran Kumar, A. S. Recent shallow moonquake and impact-triggered

569 boulder falls on the Moon: New insights from the Schrödinger basin. *J. Geophys. Res.: Planets* 121,
570 147-179, 2016.

571 Landgraf, M., Carpenter, J., Sawada, H. HERACLES Concept: An International Lunar Exploration
572 Architecture Study. Lunar Exploration Analysis Group. Abstract 2039, 2015.

573 Loftin, K., Griffith, C.T., Kidd, R., Niedholdt, E., Kibelka, G., Wright, K. Integration and Ruggedization of a
574 Commercially Available Gas Chromatograph and Mass Spectrometer (GCMS) For The Resource
575 Prospector Mission (RPM). Harsh Environment Mass Spectrometry Workshop presentation, 2013.

576 Longhi, J., Walker, D., Grove, T. L., Stolper, E. M., Hays, J. M. The petrology of the Apollo 17 mare basalts.
577 *Proc. Lunar Sci. Conf. 5th*, pp. 447-469, 1974.

578 Lucey, P.G., Blewett, D.T., Hawke, B.R. Lunar iron and titanium abundance algorithms based on final
579 processing of Clementine ultraviolet-visible images. *J. Geophys. Res.* 105 (E8), 20297-20305, 2000.

580 NASA Space Science Data Center. Document 1970-095A, 1970.

581 NASA Space Science Data Center. Document 1973-001A, 1973.

582 Malin, M.C., Bell, J.F., Cameron, J., Dietrich, W.E., Edgett, K., Hallet, B., Herkenhoff, K.E., Lemmon, M.T.,
583 Parker, T.J., Sullivan, R.J., Sumner, D.Y., Thomas, P.C., Wohl, E.E., Ravine, M.A., Caplinger, M.A. and
584 Maki, J.N. The mast cameras and Mars descent imager (MARDI) for the 2009 Mars Science
585 Laboratory. Lunar and Planetary Science Conference XXXVI. Abstract 1214, 2005.

586 Martin, D. J. P., McDonald, F. E., Steenstra, E. S., Paisarnsombat, S., Venturino, C. S., O'Hara, S., Calzada-
587 Diaz, A., Leader, M. K., Bottoms, S., Klaus, K. K., Hurwitz-Needham, D., Kring, D. A. A long duration
588 human-assisted robotic sample return mission to the Schrödinger basin part 2: traversing towards
589 the basin wall. Lunar and Planetary Science Conference 47. Abstract 1468, 2016.

590 McDonald, F. E., Martin, D. J. P., Steenstra, E. S., Paisarnsombat, S., Venturino, C. S., O'Hara, S., Calzada-
591 Diaz, A., Leader, M. K., Bottoms, S., Klaus, K. K., Hurwitz-Needham, D., Kring, D. A. A long duration
592 human-assisted robotic sample return mission to the Schrödinger basin part 1: traversing the basin
593 center. Lunar and Planetary Science Conference 47. Abstract 1464, 2016.

594 Meyer, C., Jr., McKay, D.S., Anderson, D.H., Butler, P., Jr. The source of sublimates on the Apollo 15
595 green and Apollo 17 orange glass samples. *Proc. Lunar Sci. Conf. 6th*, p. 1673-1699, 1975.

596 Mitchell, J.K., Houston, W.N., Scott, R.F., Costes, N.C., Carrier, W.D., Bromwell, L.G. Mechanical
597 properties of lunar soil: Density, porosity, cohesion, and angle of internal friction. *Proc. Lunar Sci.*
598 *Conf. Proc. 3rd*, GCA, 3, 3235-3253, 1972.

599 Mitchell, J.K , Carrier, III, W.D., Costes, N.C., Houston, W.N., Scott, R.F., Hovland, H.J. Chapter 8: Soil
600 mechanics. In: Apollo 17 Preliminary Science Report. Scientific and Technical Information Office,
601 NASA, Washington D.C., 1973.

602 Moore, H.J. Estimates of the mechanical properties of lunar surface using tracks and secondary impact
603 craters produced by blocks and boulders (No. 70-229). US Dept. of the Interior, Geological Survey,
604 65 p, 1970.

605 Morrison, R.H., Oberbeck, V.R. A composition and thickness model for lunar impact crater and basin
606 deposits. Lun. Planet. Sci. Conf. Proc. 9th, 3763-3785, 1978.

607 Myrick, T.M., Davis, K., Wilson, J. Rock Abrasion Tool. 37th Aerospace Mechanisms Symposium, pp. 277-
608 290, 2004.

609 Myrick, T.M., Pham, T.T., Kalanick, M.F. Rock Core Capture and Caching Technique. In: International
610 Workshop on Instrumentation for Planetary Missions. LPI Contribution No. 1683, p. 1118, 2012.

611 National Research Council. The scientific context for exploration of the Moon, Final Report. National
612 Academies Press, Washington, DC, pp. 120, 2007.

613 O'Sullivan, K.M., Kohout, T., Thaisen, K.G., Kring, D.A. Calibrating several key lunar stratigraphic units
614 representing 4 b.y. of lunar history within Schrödinger basin, in: Williams, D. A., Ambrose, W. (Eds),
615 *Recent Advances in Lunar Stratigraphy. Geological Society of America Special Paper 477*, Boulder,
616 CO., pp. 117-127, 2011.

617 Oberbeck, V.R., Hörz, F., Morrison, R.H., Quaide, W.L., Gault, D.E. On the origin of the lunar smooth-
618 plains. *The Moon*, 12(1), 19-54, 1975.

619 Paulsen, G., Zacny, K., Steele, A., Conrad, P., Chu, P., Hedlund, M., Craft, J., McCarthy, T., Schad, C.
620 Demonstration of the Acquisition and Caching for the Mars Sample Return Missions. Lunar and
621 Planetary Science Conference XLIII Abstract 1151, 2012.

622 Petrov, G. I. Investigation of the Moon with the Lunokhod 1 space vehicle. In: *COSPAR Space Research*
623 *XII*, pp. 1-12. Akademie-Verslag, Berlin, 1972.

624 Potts, N.J., Gullikson, A.M., Curran, N.M., Dhaliwal, J.K., Leader, M.K., Rege, R.N., Klaus, K.K., Kring, D.A.
625 Robotic traverse and sample return strategies for a lunar farside mission to the Schrödinger basin.
626 *Adv. Space Res.* 55, 1241-1254, 2015.

627 Pratt, W., Alkalai, L., Buxton, C., Drever, M., Hall, S., Hopkins, J.B., Ringelberg, J., Scott, A. Human-
628 assisted sample return from the Moon and Mars using the Orion spacecraft. International
629 Astronautical Congress, IAC-13-A5.1.7, 2014.

630 Rieder, R., Gellert, R., Bruckner, J., Klingelhofer, G., Dreibus, G., Yen, A., Squyres, S.W. The new Athena
631 alpha particle X-ray spectrometer for the Mars Exploration Rovers. *J. Geophys. Res.: Planets* 108,
632 8066-8078, 2003.

633 Rutherford, M.J., Papale, P. Origin of basalt fire-fountain eruptions on Earth versus the Moon. *Geology*
634 37, 219-222, 2009.

635 Seeni, A., Schäfer, B., Hirzinger, G. Robot mobility systems for planetary surface exploration: state-of-
636 the-art and future outlook: a literature survey. In Thawar, T. Arif (Eds.), *Aerospace Technologies*
637 *Advancements*, Chapter 10, pp. 189-208, ISBN: 978-953-7619-96-1, 2010.

638 Shearer, C., Neal, C., Borg, L., Jolliff, B., Papanastassiou, D., Treiman, A., Floss, R., Rutherford, M.,
639 Norman, M., Farquhar, J. Analysis of lunar sample mass capability for the lunar exploration
640 architecture. Unpublished white paper, 12p, posted May 2007 by the Curation and Analysis Planning
641 Team for Extraterrestrial Materials (CAPTEM). <http://www.lpi.usra.edu/captem/>.

642 Shearer, C., Tahu, G. Lunar Polar Volatiles Explorer (LPVE). NASA Mission Concept Study, 2010.

643 Shoemaker, E. M., Robinson, M.S., Eliason, E.M. The South Pole Region of the Moon as Seen by
644 Clementine. *Science* 266, 1851-1854, 1994.

645 Stolper, E. M. Apollo 15 green glass. A.B. thesis, Harvard University. 178 pp, 1974.

646 Terzaghi, K. Theoretical soil mechanics. New York, John Wiley and Sons, Inc., p. 509, 1948.

647 Tian, B. Y., Poole, W. D., Garber, J. M., French, R. A., Smith, P. H., Barnes, J. J., Kring, D. A. Landing sites
648 optimized for geophysical studies of the structure and thermal state of the lunar interior. Lunar
649 Planetary Science Conference XLIV. Abstract 1629, 2013.

650 Trask, N.J. Geologic comparison of mare materials in the lunar equatorial belt, including Apollo 11 and
651 Apollo 12 landing sites. *U.S. Geol. Surv. Prof. Pap.*, 750D, 138-148, 1971.

652 Vaughan, W.M., Head, J.W., Wilson, L., Hess, P.C. Geology and petrology of enormous volumes of impact
653 melt on the Moon: A Case study of the Orientale basin impact melt sea. *Icarus* 223, 749-765, 2013.

654 Venturino, C.S., Martin, D. J. P., McDonald, F. E., Paisarnsombat, S., Steenstra, E. S., O'Hara, S., Calzada-
655 Diaz, A., Bottoms, S., Leader, M. K., Klaus, K. K., Gregg, T. K. P., Kring, D.A. Lunar pyroclastic soil
656 mechanics and trafficability in the Schrödinger basin. Lunar Planetary Science Conference 47.
657 Abstract 1676, 2016.

658 Walker, D., Kirkpatrick, R. J., Longhi, J., Hays, J. F. Crystallization history of lunar picritic basalt sample
659 12002: Phase equilibria and cooling rate studies. *Geol. Soc. Am. Bull.* 87, 646-656, 1976.

660 Wieczorek, M., Mimoun, D., Baratoux, D., Bouley, S., Cecconi, B., Collins, G., Cook, A., Crawford, I.,
661 Dehant, V., Falcke, H., Garcia, R., Giardini, D., Grimm, R., Grott, M., Grygorczuk, J., Gurtvis, L., Ivanov,

662 B., Jaumann, R., Josset, J-L., Klein-Wolt, M., Kletetschka, G., Koopmans, L., Langlais, B., Lawrence, D.,
663 Lognonne, P., Margonis, A., Meslin, P-Y., Neal, C., Oberst, J., Ripka, P., Schmitz, N., Spohn, T., Werner,
664 S., Zarka, P. Farside: A mission to the farside of the Moon. ESA mission proposal, 2015.
665 Wetzell, D.T., Hauri, E.H., Saal, A.E., Rutherford, M.J. Carbon content and degassing history of the lunar
666 volcanic glasses. Nature Geoscience doi:10.1038/ngeo2511, 2015.
667 Wilhelms, D., Howard, K., Wilshire, H. Geological Map of the South Side of the Moon. U.S. G.S.
668 Miscellaneous Investigative Series Map I-1162, 1979.
669 Zacny,, K., Craft, J., Hedlund, M., Wilson, J., Chu, P., Fink, P., Mueller, R., Galloway, G., Mungas, G. Novel
670 Approaches to Drilling and Excavation on the Moon. American Institute Of Aeronautics and
671 Astronautics Conference. Abstract 2009-6431, 2009.
672 Zacny, K., Chu, P., Paulsen, G., Craft, J. Core acquisition and caching for the 2020 Mars mission. Lunar
673 and Planetary Science Conference XLIV. Abstract 1331, 2013.
674 Zacny, K., Conrad, P., Mahaffy, W., Brinckerhoff, W., Steele, A., Blake, D., Anderson, S. Concepts and
675 Approaches for Mars Exploration. Abstract 4282, 2012.

676

677 **Figure captions**

678

679 **Fig. 1.** Maps of Schrödinger basin showing (A) the WAC image and (B) the WAC image with overlain
680 geological map of Kramer et al. (2013) with brown (*Ep*) = pyroclastic material, red (*Em*) = inter-basin
681 mare material, purple (*Isc*) = secondary crater field, dark purple (*Imp*) = impact melt ponds, from light to
682 dark blue: *Isip* = smooth inner-peak ring floor material, *Isds* = spectrally distinct smooth floor material,
683 *Isop* = smooth outer-peak ring floor material, *Ish* = smooth hummocky floor material, *lipr* = inter-peak
684 ring floor material, *lrh* = rough hummocky floor material, light brown (*lw*) = wall material, horizontally
685 dashed = wall slump, vertically dashed = peak ring slump and yellow (*pNpr*) = peak ring material.

686

687 **Fig. 2.** Schematic overview of Schrödinger basin showing the major geological units and surface
688 morphology with a topographic, vertical exaggeration of ~3. Range of pyroclastic source depths based
689 on Delano (1980), Stolper (1974), Green and Ringwood (1973) and range of mare basalt source depths
690 based on Walker et al. (1976) and Longhi et al. (1974).

691

692 **Fig. 3.** The identified boulders and trails (detail of NAC images M141351170LE, M141357955LE) within
693 the pyroclastic material that were used to determine the bearing capacity of the pyroclastic deposits.

694

695 **Fig. 4.** Short traverse. Maps were generated in ArcGIS® using WAC imagery (A) The short traverse
696 overlain by the geological map of Kramer et al. (2013). The three landing sites are indicated with yellow
697 filled circles, in-situ analysis stations with open red circles and sampling stations with red filled
698 circles. Brown (*Ep*) = pyroclastic material, red (*Em*) = inter-basin mare material, purple (*lsc*) = secondary
699 crater field, light blue (*lrip*) = smooth inner-peak ring floor material, dark blue (*lipr*) = inter-peak ring
700 floor material and yellow (*pNpr*) = peak ring material. (B) The short traverse overlain by the slope map
701 based on LOLA data.

702

703 **Fig. 5.** Views along the short traverse. The 3D views were created using LRO NAC images overlain on
704 LOLA topography data using ArcScene©. (A) Oblique view of the stations along the peak ring area based
705 on LRO NAC images M108293032LE-RE, M110650294LC-RE, M113006586RC, M167289673LC,
706 M169650959LC and M174368352RC (B) Boulder identified at station S5. (C) Oblique view of the fracture
707 north of the peak ring area. (D) Top down view of the fracture at station S6. (E) Station S32 with a ~5 m
708 boulder, diameter of crater is 220 m.

709

710 **Fig. 6.** Schematic cross-section of the pyroclastic vent in Schrödinger basin based on LOLA topographical
711 data and surface geological units from Kramer et al. (2013). It shows a volatile-driven fire-fountain type
712 of eruption, upon which the melt droplets are quenched to glass bead and subsequently coated by
713 condensation of volatile-rich vapors. Source depth estimates based on Delano (1980), Stolper (1974) and
714 Green and Ringwood (1973).

715

716 **Fig. 7.** Plot showing the estimated primary material within the secondary ejecta deposit (in wt.%) as a
717 function of the secondary crater diameter.

718

719 **Fig. 8.** Long traverse. Maps generated in ArcGIS© using WAC imagery. The three landing sites are
720 indicated with yellow filled circles, in-situ analysis stations with open red circles and sampling stations
721 with red filled circles. The dashed line is an optional route close to the volcanic vent. (A) The long
722 traverse overlain by the geological map of Kramer et al. (2013) with brown (*Ep*) = pyroclastic material,
723 purple (*lsc*) = secondary crater field, from lighter to darker blue: *lrip* = smooth inner-peak ring floor
724 material, *lipr* = inter-peak ring floor material, *lsh* = smooth hummocky floor material, light brown (*lw*) =
725 wall material, horizontally dashed = wall slump and yellow (*pNpr*) = peak ring material. (B) The long

726 traverse overlain by the slope map based on LOLA data and corresponding elevation profile of the long
727 traverse.

728

729 **Fig. 9.** Views from the long traverse. The 3D views were created using LRO NAC images overlain on LOLA
730 topography data using ArcScene©. (A) View inside the pyroclastic vent from the long traverse. (B-C)
731 Overview of station L19 showing a ~1.1 km boulder track. The boulder originated from an outcrop
732 higher up slope. (D) Overview of the SE wall area and the stations identified within this area. (E) The SE
733 wall area overlain by M³ data (Kramer et al., 2013). (F) Station L44 showing outcrops of noritic lithologies
734 based on M³ data (Kramer et al., 2013). (G) Station L48 situated close to a boulder field of pyroxene-
735 bearing anorthositic material, based on M³ data (Kramer et al., 2013).

APPENDIX A.

Appendix for “Analyses of Robotic Traverses and Sample Sites in the Schrödinger basin for the HERACLES Human-Assisted Sample Return Mission Concept” by E.S. Steenstra, D.J.P. Martin, F.E. McDonald, S. Paisarnsombat, C. Venturino, S. O’Hara, A. Calzada-Diaz, M.K. Leader, K.K. Klaus, W. van Westrenen, D. H. Needham, D.A. Kring.

1. Details on traverse stations

Tables S.1. and S.2. list the sampling stations that were identified along the short and long traverse, respectively. Included are the location, type of sample and mass, type of in-situ analyses and scientific goals that can be addressed at the identified stations along each traverse. The amount of sampling stations were based on the assumption of a notional baseline of <30 kg of total returned sample mass.

2. Calculations of sample mass capabilities of sample container spheres

The maximum sample mass that can be returned from the lunar surface is constrained by the volume of the sample transport container that is required for exchanging the samples from the lander to the exploration Deep Space Habitat (eDSH) and subsequently to the Orion crew vehicle. Current designs include spherical sample containers with variable diameters dependent on their mission context (Pratt et al., 2014). However, the technical specifications (e.g., wall thickness) of these containers are not known. We therefore consider a simple scenario assuming spheres with variable internal diameters and calculate the volumes that would be required for various sample suites (Fig. S.1). Because of the current uncertainty in the sample mass that may be returned to Earth, an arbitrary maximum sample mass of 10 kg per ascent was considered in this study. This is a baseline limit given the lander ascent mass capability presented in this work and additional returned samples would significantly increase the overall productivity of a robotic mission to Schrödinger basin. The different lunar lithologies exhibit a wide range of densities and therefore we assume the associated densities of 3.0-3.3 g/cm³ for basaltic lithologies (Kiefer et al., 2012), 2.0-2.6 g/cm³ for impact melt breccias (Warren, 2001; Macke et al., 2012), 1.3-1.8 g/cm³ for lunar regolith (Mitchell et al., 1972) and 2.6-3.7 g/cm³ for homogeneous rocks that include anorthosites, norites and dunites. We then calculated the mass capability of the sample container sphere that would be required to accommodate the sampled lithologies along each section of the traverse (Table S.3, Fig. S.1).

3. Calculation of ascent vehicle payload capabilities

To assess how much sample mass can be returned from the lunar surface, we designed a baseline, reusable ascent vehicle based on the dimensions of the JPL Mars Ascent Vehicle (MAV). The ascent vehicle has a length of 2.56 meters, a diameter of 0.442 meters, and a mass (with a 30% contingency) of 80 kg (Stephenson and Willenberg, 2006; Dux et al., 2011). A maximum ΔV of 2,434 m/s was shown to be sufficient for an ascent vehicle to travel from the lunar surface to Orion in an EM-L2 orbit, EM-L2 halo orbit, or distant retrograde orbit (DRO) (Pratt et al., 2014). The proposed traverses in this study were based notional sample payload of 10 kg per ascent, that has been shown to be the minimum required sample mass that is able to successfully capture important geological samples. We also have shown that this payload is the baseline, and that more returned sample mass would greatly increase the overall productivity of the mission. Four different engines were examined for this ascent vehicle study. Only liquid fuel engines of an appropriate size were selected due to the HERACLES architecture that requires a reusable ascent vehicle. Eqs. (A.1, A.2) were used to calculate the maximum payload for the given ΔV :

$$\Delta V = v_e \ln(PMF) \tag{A.1}$$

$$PMF = \frac{Full\ Mass}{Empty\ Mass} \quad (A.2)$$

in which ΔV is the change in velocity (m/s), V_e is the exhaust velocity (m/s) and PMF is the propellant mass fraction. Figure S.2 shows the maximum payload as a function of ascent vehicle volume for each engine type. These calculations suggest the MAV has the ability to lift payload far exceeding 10 kg. Additional calculations were then performed to determine the minimum ascent vehicle engine volume that is required to lift off 10 kg of sample payload from the lunar surface. This requires selection of a certain engine type and type of propellant. The Aestus II, a collaboration between Ottobrunn Space Propulsion Centre and Rocketdyne, seems to be most suited for a reusable ascent vehicle of the size considered in this study. Monomethylhydrazine (MMH) was determined to be the best propellant for storage and refueling due to its relatively high boiling point and low freezing point. Of the engines we considered which use MMH, the Aestus II has the highest ISP and thrust (Table S.4) Propellant storage is also important to consider because of the 3-year mission length of the HERACLES mission concept and the potential for the ascent vehicle to sit on the lunar surface for long periods of time. When the Aestus II engine is considered, we observe that the initial estimate for the size of the ascent vehicle is larger than required for a 11 kg payload (10 kg of samples and 1 kg of packaging). Figure S.3. shows the estimated ascent vehicle dimensions for a wider range of payloads (in this case sample masses).

4. Qualitative assessment of crater degradation states

Evaluation of the ages of the sampled primary craters along the traverses is essential for determining the recent (post-Imbrian) impact flux. We therefore assessed the age of small (<10 km diameter) primary craters sampled along the traverse using the crater degradation model of Trask (1971). This model is a simple approach that is based on the various degradation states of primary craters due to space weathering over time. We observe that although both traverses will yield samples from relatively young craters, the medium traverse is expected to provide a wider range of sampled crater ages and potentially better calibration of the post-Imbrian impact flux (Fig. S.4.).

5. Soil mechanics and rover trafficability

Figure S.5. shows the boulder tracks which were used in the calculations related to assessment of rover trafficability in the pyroclastic deposits (see main text). Details on the calculations are provided in Tables S.5-S.7.

6. Communication and returning HD imagery of the lunar surface

Returning HD imagery is of great importance for the educational and promotional yields of planetary exploration (e.g., the Kaguya mission, Terazono et al., 2009). Here, we assess the possibility of returning HD imagery from the lunar surface to eDSH, and subsequently from the eDSH to ground stations on Earth.

6.1 Communication between rover and eDSH

Communication between the rover and the eDSH is likely to occur through KA band system, which is currently the most feasible way of communication as there is currently no funding for a dedicated farside communications-relay satellite in an Earth-Moon L2 halo orbit (Pratt et al., 2014). Current mission designs require a high data rate from the rover to the EAM that allows for transmitting high quality (HD) imagery and/or video. However, the data transfer rate between the rover and the EAM may be limited to approximately 200-400 kbps at their average separation distance - approximately ~60,000 km from the lunar surface to the EM-L2 halo orbit (Pratt et al., 2014). Direct transmission of 720p HD video would require ~5 mbps, far exceeding the estimated data transfer rate. High-definition imagery

and/or videos must therefore be transferred at much lower speeds. To determine the feasibility of transmitting stored HD imagery and/or video from the rover, knowledge of the communication data rates during different rover operation modes is required. During traversing, the rover-eDSH communications data rate will be ~89 kbps as it requires continuous operation of the two Hazcams and the Ground Penetrating Radar (Table 1, main text). During stationary analyses, data rates will be significantly lower. For example during APXS analysis, the Hazcams and GPR can be turned off allowing for the transfer of HD imagery and/or videos stored on the rover.

6.2 Communication between eDSH and ground stations on Earth

For the communication between the eDSH and ground stations on Earth we performed a trade study between KA-band or laser communication. Laser communication has heritage on the Laser Lunar Communication Demonstration (LLCD) on the Lunar Atmospheric and Dust Environment Explorer (LADEE) mission, whereas KA-band communication has heritage on many missions (e.g., Kepler, the Lunar Reconnaissance Orbiter and military satellites). However, improvements in laser communication has been identified as an important technology development for future deep space exploration, because it has the potential to deliver data rates that far exceeds those using KA-band (e.g., Boroson and Robinson, 2014). Laser communication also requires half the power that is used for KA-band (Table S.8.). However, for a robotic mission to the lunar surface the distance between the eDSH and the Earth is insufficiently large for significant delays for KA-band communication. In addition, clouds may have a significant effect on laser communication. For example, thin cloud coverage can potentially reduce the data rate to 77 Mbps (Cornwell et al., 2014). The use of laser communication would also require more ground stations on Earth's than currently available. We conclude that, given the amount of data that would need to be transferred to support HD imagery and the heritage of both types of communication, KA-band is sufficient and less costly for communication between the eDSH and ground stations on Earth.

Supplementary references

- Boroson, D. M., Robinson, B. S. The Lunar Laser Communication Demonstration: NASA's First Step Toward Very High Data Rate Support of Science and Exploration Missions. *Space Sci. Rev.*, 185, 115-128, 2014.
- Cornwell, D., Boroson, D., Robinson, B., Burianek, D., Murphy, D., Khatri, F. The Lunar Laser Communication Demonstration (LLCD). Presentation to JHU Aerospace Affinity Group. <<http://alumni.jhu.edu/sites/default/files/NASA-LasercomTalk-JHU-Aerospace-Affinity-June-11th-2014.pdf>>, 2014.
- Dux, I. J., Huwaldt, J. A., Mckamey, R. S., Dankanich, J. W. Mars Ascent Vehicle Gross Lift-off Mass Sensitivities for Robotic Mars Sample Return. NASA/TM-2011-216968, 2011.
- Hurwitz, D. M., Kring, D. A. Potential sample sites for South Pole-Aitken basin impact melt within the Schrödinger basin. *Earth Planet. Sci. Lett.* 427, 31-36, 2015.
- Kiefer, W. S., Macke, R. J., Britt, D. T., Irving, A. J., Consolmagno, G. J. Regional variability in the density of lunar mare basalts and implications for lunar gravity modeling. Lunar and Planetary Science Conference Proceedings. Abstract 1642, 2012.
- Kramer, G. Y., Kring, D. A., Nahm, A. L., Pieters, C. M. Spectral and photogeologic mapping of Schrödinger Basin and implications for post-South Pole-Aitken impact deep subsurface stratigraphy. *Icarus* 223, 131-148, 2013.
- Macke, R. J., Kiefer, W. S., Britt, D. T., Irving, A. J., Consolmagno, G. J. Density and Porosity of Apollo Lunar Basalts and Breccias. Lunar and Planetary Science Conference 43. Abstract 1299, 2012.
- Mitchell, J. K., Houston, W. N., Scott, R. F., Costes, N. C. Mechanical properties of lunar soil: density, porosity, cohesion, and angle of internal friction. Proceedings of the Third Lunar Science Conference 3235-3253, 1972.

- National Research Council. The scientific context for exploration of the Moon, Final Report. National Academies Press, Washington, DC, pp. 120, 2007.
- Pratt, W., Alkalai, L., Buxton, C., Drever, M., Hall, S., Hopkins, J. B., Ringelberg, J., Scott, A. Human-assisted sample return from the Moon and Mars using the Orion spacecraft. 65th IAC, 13-A5.1.7., 2014.
- Shearer, C., Neal, C., Borg, L., Jolliff, B., Papanastassiou, D., Treiman, A., Floss, R., Rutherford, M., Norman, M., Farquhar, J., Analysis of lunar sample mass capability for the lunar exploration architecture. Unpublished white paper, 12p, posted May 2007 by the Curation and Analysis Planning Team for Extraterrestrial Materials (CAPTEM). <<http://www.lpi.usra.edu/captem/>>
- Stephenson, D. D., Willenberg, H. J. Mars Ascent Vehicle: Key Elements of a Mars Sample Return Mission. IEEEAC. Abstract 1009, 2006.
- Terazono, J., Yoshikawa, M., Wakabayashi, N. Space Education Strategy Using Data Obtained by Lunar and Planetary Missions. Trans. JSASS Space Tech. Japan., 7, Tu_25-Tu_29, 2009.
- Trask, N. J. Geologic comparison of mare materials in the lunar equatorial belt, including Apollo 11 and Apollo 12 landing sites. U.S. Geol. Surv. Prof. Pap., 750D, 138-148, 1971.
- Warren, P. H. Porosities of lunar meteorites: Strength, porosity, and petrologic screening during the meteorite delivery process. J. Geophys. Res. 106, 10101-10111, 2001.
- Willhelms, D. E. The Moon. In: *The Geology of the Terrestrial Planets* (M. Carr et al., eds.), pp. 107-205. NASA SP-469, 1984.

Table S.1. Summary of location, type of sample and mass, type of in-situ analyses and scientific goals (NRC, 2007) that can be addressed at the identified stations of the short traverse assuming a notional baseline of <30 kg of total returned sample mass

	Latitude	Longitude	Elevation (m)	Lithological unit ¹	Sample type and mass (g) ²	Scientific goals addressed ³
Landing site 1	-75.4050	141.1768	-4733			
<i>Station S1</i>	-75.4907	141.3745	-4723	Ep	Regolith (2000)	2b, 2d, 5c, 5d, 7b, 7c
<i>Station S2</i>	-75.4906	142.0473	-4541	pNpr	Boulder (500) ^a	2a, 3a, 3b, 3c, 3d
<i>Station S3</i>	-75.3983	142.1327	-4520	pNpr	Boulder (500) ^a	2a, 3a, 3b, 3c, 3d
<i>Station S4</i>	-75.3651	142.1738	-4465	pNpr	Boulder (N/A)	2a, 3a, 3b, 3c, 3d
<i>Station S5</i>	-75.2628	142.2408	-4506	pNpr	Boulder (500) ^a	2a, 3a, 3b, 3c, 3d
<i>Station S6</i>	-75.1507	141.9541	-4820	Ep/pNpr	Mixed rake (1000)	2a, 2b, 2d, 3a, 3b, 3c, 3d, (4a, 4b, 4c), 5c, 5d
<i>Station S7</i>	-75.2560	141.8327	-4651	lipr	Boulder (N/A)	6c
<i>Station S8</i>	-75.3027	141.9196	-4618	lipr	Boulder (5000) ^b	1a, 1c, 1d, 6c
<i>Station S9</i>	-75.4149	141.4296	-4740	Ep	Regolith (N/A)	2b, 2d, 5c, 5d, 7b, 7c
Landing site 1	-75.4050	141.1768	-4733		(Total: 9.5 kg)	
<i>Station S10</i>	-75.3602	140.9211	-4706	Ep	Boulder (N/A)	2b, 2d, 5c, 5d, 6c, 6d
<i>Station S11</i>	-75.3370	140.8480	-4734	Ep	Regolith (N/A)	2b, 2d, 5c, 5d, 6c, 6d, 7b, 7c
<i>Station S12</i>	-75.3121	140.4326	-4590	Ep	Boulder (N/A)	2b, 2d, 5c, 5d, 6c
<i>Station S13</i>	-75.2946	140.3430	-4586	Ep	Regolith (N/A)	2b, 2d, 3b, 5c, 5d, 7b, 7c
<i>Station S14</i>	-75.2554	140.2323	-4572	Ep	Regolith (2000)	1d, 2b, 2d, 5c, 5d, 7b, 7c
<i>Station S15</i>	-75.1561	140.1177	-4538	Ep	Boulder (N/A)	2b, 2d, 5c, 5d, 6c
<i>Station S16</i>	-75.0817	140.1110	-4586	Ep	Boulder (N/A)	2b, 2d, 5c, 5d, 6c
<i>Station S17</i>	-75.0749	140.1027	-4590	Ep	Regolith (N/A)	2b, 2d, 5c, 5d, 6c, 7b, 7c
<i>Station S18</i>	-75.0287	140.2267	-4634	Ep	Regolith (N/A)	2b, 2d, 5c, 5d, 6c, 7b, 7c
<i>Station S19</i>	-74.9926	140.2379	-4654	Ep	Regolith (N/A)	2b, 2d, 5c, 5d, 6c, 7b, 7c
<i>Station S20</i>	-74.9580	140.1913	-4676	Ep	Regolith (N/A)	2b, 2d, 5c, 5d, 6c, 7b, 7c
<i>Station S21</i>	-74.9087	140.0887	-4746	Ep	Regolith (N/A)	2b, 2d, (4a, 4b, 4c), 5c, 5d, 7b, 7c
<i>Station S22</i>	-74.8699	139.1497	-4664	Ep	Regolith (N/A)	2b, 2d, 5c, 5d, 6c, 7b, 7c
<i>Station S23</i>	-74.8453	139.0352	-4660	Ep	Boulder (N/A)	2b, 2d, 5c, 5d, 6c
<i>Station S24</i>	-74.8570	138.7690	-4650	Ep	Regolith (2000)	1d, 1e, 2b, 2d, 5c, 5d, 6c, 7b, 7c
<i>Station S25</i>	-74.7741	138.8835	-4710	Ep	Boulder (N/A)	2b, 2d, 5c, 5d, 6c
<i>Station S26</i>	-74.5854	138.7655	-4767	Ep	GPR (N/A)	5c, 7b, 7c
<i>Station S27</i>	-74.5501	138.7259	-4801	Ep/Isip	GPR (N/A)	5c, 7b, 7c
<i>Station S28</i>	-74.5186	138.6371	-4804	Ep/Isip	GPR (N/A)	5c, 7b, 7c
<i>Station S29</i>	-74.2082	138.1795	-4821	Isip	Boulder (N/A)	6a, 6c, 6d
<i>Station S30</i>	-74.1183	138.1210	-4779	Isip	Boulder (N/A)	6a, 6c, 6d
<i>Station S31</i>	-73.8455	137.5857	-4835	Em	Regolith (500)	2b, 2d, 3a, 3b, 5a, 5b, 5d, 7b, 7c
<i>Station S32</i>	-73.9664	136.4695	-4775	Isip	Boulder (5000) ^b	1a, 1c, 1e, 6a, 6c, 6d
<i>Station S33</i>	-74.1203	134.7569	-4784	Em	Regolith (500)	2b, 2d, 3a, 3b, 5a, 5b, 5d, 7b, 7c
Landing site 2	-74.0760	134.5498	-4778		(Total: 10.0 kg)	
<i>Station S34</i>	-74.0478	133.8572	-4776	Em/Isip	Boulder (N/A)	2b, 2d, 3a, 3b, 5a, 5b, 5d
<i>Station S35</i>	-74.0383	133.6015	-4782	Isip	Boulder (N/A)	6a, 6c, 6d
<i>Station S36</i>	-74.0420	133.5345	-4792	Isip	Boulder (N/A)	6a, 6c, 6d
<i>Station S37</i>	-74.0455	133.5285	-4796	Em/Isip	Boulder (500)	2b, 2d, 3a, 3b, 5a, 5b, 5d, 6a, 6c, 6d
<i>Station S38</i>	-74.0520	133.4926	-4805	Em/Isip	Boulder (500)	2b, 2d, 3a, 3b, 5a, 5b, 5d, 6a, 6c, 6d
<i>Station S39</i>	-74.0743	133.4241	-4811	Em	Regolith (N/A)	2b, 2d, 3a, 3b, 5a, 5b, 7b, 7c
<i>Station S40</i>	-74.0941	133.3957	-4810	Em	Boulder (N/A)	2b, 2d, 3a, 3b, 5a, 5b
<i>Station S41</i>	-74.1973	133.3561	-4786	Em/Isip	Boulder (N/A)	2b, 2d, 3a, 3b, 5a, 5b, 6a, 6c, 6d
<i>Station S42</i>	-74.2370	132.9933	-4775	Em/Isip	Regolith (N/A)	2b, 2d, 3a, 3b, 5a, 5b, 6a, 6c, 6d, 7b, 7c
<i>Station S43</i>	-74.2655	132.9633	-4752	Em/Isip	Boulder (N/A)	2b, 2d, 3a, 3b, 6a, 6c, 6d
<i>Station S44</i>	-74.3108	132.8374	-4736	Isip	Boulder (N/A)	6a, 6c, 6d
<i>Station S45</i>	-74.4394	132.9465	-4673	Isip	Mixed rake (333)	1a, 1c, 1e, 3d, 6a, 6c, 6d
<i>Station S46</i>	-74.4998	133.4288	-4703	Isip	Mixed rake (333)	1a, 1c, 1e, 3d, 6a, 6c, 6d
<i>Station S47</i>	-74.6019	133.3457	-4676	Isip	Mixed rake (333)	1a, 1c, 1e, 3d, 6a, 6c, 6d
<i>Station S48</i>	-74.8181	133.4272	-4642	Isip	Boulder (5000) ^b	1a, 1c, 1e, 6a, 6c, 6d
<i>Station S49</i>	-74.9557	133.0139	-4481	Isip	Regolith (2000)	1a, 1c, 2a, 2b, 2d, 3a, 3b, 3c, 3d, 5a, 5b, 5d, 6a, 7b, 7c
<i>Station S50</i>	-75.0866	133.3906	-4595	Isip	Regolith (N/A)	2a, 2b, 2d, 3a, 3b, 3c, 3d, 5a, 5b, 6a, 7b, 7c
Landing site 3	-75.1710	133.3401	-4587		(Total: 9.0 kg)	
					(Traverse total: 28.5 kg)	

^aBased on M3 spectra considered to be a crystalline, homogeneous rock (sample mass after Shearer et al., 2007)

^bAssumed to be heterogeneous impact melt breccia (sample mass after CAPTEM, 2007)

¹Kramer et al. (2013) ²Based on CAPTEM recommendations (Shearer et al., 2007) ³NRC (2007)

Table S.2. Summary of location, type of sample and mass, type of in-situ analyses and scientific goals (NRC, 2007) that can be addressed at the identified stations of the long traverse assuming a notional baseline of <30 kg of total returned sample mass

	Latitude	Longitude	Elevation (m)	Lithological unit ¹	Sample type and mass (g) ²	Scientific goals addressed ³
Landing site 1	-75.4050	141.1768	-4733			
<i>Station S1</i>	-75.4907	141.3745	-4723	Ep	Regolith (2000)	2b, 2d, 5c, 5d, 7b, 7c
<i>Station S2</i>	-75.4906	142.0473	-4541	pNpr	Boulder (500) ^a	2a, 3a, 3b, 3c, 3d
<i>Station S3</i>	-75.3983	142.1327	-4520	pNpr	Boulder (500) ^a	2a, 3a, 3b, 3c, 3d
<i>Station S4</i>	-75.3651	142.1738	-4465	pNpr	Boulder (N/A)	2a, 3a, 3b, 3c, 3d
<i>Station S5</i>	-75.2628	142.2408	-4506	pNpr	Boulder (500) ^a	2a, 3a, 3b, 3c, 3d
<i>Station S6</i>	-75.1507	141.9541	-4820	Ep/pNpr	Mixed rake (1000)	2a, 2b, 2d, 3a, 3b, 3c, 3d, (4a, 4b, 4c), 5c, 5d
<i>Station S7</i>	-75.2560	141.8327	-4651	lipr	Boulder (N/A)	6c
<i>Station S8</i>	-75.3027	141.9196	-4618	lipr	Boulder (5000) ^b	1a, 1c, 1d, 6c
<i>Station S9</i>	-75.4149	141.4296	-4740	Ep	Regolith (N/A)	2b, 2d, 5c, 5d, 7b, 7c
Landing site 1	-75.4050	141.1768	-4733		(Total: 9.5 kg)	
<i>Station S10</i>	-75.3602	140.9211	-4706	Ep	Boulder (N/A)	2b, 2d, 5c, 5d, 6c, 6d
<i>Station S11</i>	-75.3370	140.8480	-4734	Ep	Regolith (N/A)	2b, 2d, 5c, 5d, 6c, 6d, 7b, 7c
<i>Station S12</i>	-75.3121	140.4326	-4590	Ep	Boulder (N/A)	2b, 2d, 5c, 5d, 6c
<i>Station S13</i>	-75.2946	140.3430	-4586	Ep	Regolith (N/A)	2b, 2d, 3b, 5c, 5d, 7b, 7c
<i>Station S14</i>	-75.2554	140.2323	-4572	Ep	Regolith (2000)	1d, 2b, 2d, 5c, 5d, 7b, 7c
<i>Station L1</i>	-75.3675	138.5676	-4336	Ep	Regolith (N/A)	2b, 2d, 5c, 5d, 7b, 7c
<i>Station L2</i>	-75.6870	138.6578	-4745	Ep	Boulder (N/A)	2b, 2d, 5c, 5d, 6c
<i>Station L3</i>	-75.7592	138.7186	-4735	lsc	Mixed Rake (N/A)	2b, 2d, 5c, 5d, 6a, 6c, 6d
<i>Station L4</i>	-75.7703	138.4000	-4738	lsc	Mixed Rake (N/A)	2b, 2d, 5c, 5d, 6a, 6c, 6d
<i>Station L5</i>	-75.8157	138.2629	-4668	lsc	Mixed Rake (N/A)	2b, 2d, 5c, 5d, 6a, 6c, 6d
<i>Station L6</i>	-75.8212	138.0631	-4712	Isip	Boulder (N/A)	6a, 6c, 6d
<i>Station L7</i>	-76.0064	137.7253	-4737	Isip	Regolith (N/A)	6a, 6c, 6d, 7b, 7c
<i>Station L8</i>	-76.1349	137.8276	-4698	Isip	Regolith (N/A)	6a, 6c, 6d, 7b, 7c
<i>Station L9</i>	-76.0830	138.2716	-4692	lsc	Boulder (N/A)	6a, 6c, 6d
<i>Station L10</i>	-76.1640	138.8389	-4706	lsc	Regolith (N/A)	6a, 6c, 6d, 7b, 7c
<i>Station L11</i>	-76.3181	138.6777	-4637	lsc	Boulder (N/A)	6a, 6c, 6d
<i>Station L12A</i>	-76.5039	138.4047	-4597	lsc	Boulder (5000) ^b	1a, 1c, 1d, 1e, 6a, 6c, 6d
<i>Station L12B</i>	-76.5969	139.9789	-4550	lsc	Boulder (N/A)	6a, 6c, 6d
<i>Station L13</i>	-76.7729	141.1660	-4622	Isop	Boulder (N/A)	6a, 6c, 6d
<i>Station L14</i>	-76.7558	141.3614	-4642	Isop/lsc	Boulder (N/A)	6a, 6c, 6d
<i>Station L15</i>	-76.8070	141.8635	-4683	Isop	Boulder (N/A)	6a, 6c, 6d
<i>Station L16</i>	-76.6487	142.9195	-4429	lw slump	Boulder (500)*	2a, 3a, 3b, 3c, 3d
<i>Station L17</i>	-76.8625	142.7509	-4722	lw slump	Boulder (N/A)	2a, 3a, 3b, 3c, 3d
<i>Station L18</i>	-76.8940	142.7962	-4661	lw slump	Boulder (N/A)	2a, 3a, 3b, 3c, 3d
<i>Station L19</i>	-76.9163	142.7086	-4714	lw slump	Boulder (500) ^a	2a, 3a, 3b, 3c, 3d
<i>Station L20</i>	-76.9627	142.5892	-4716	Isop/lw slump	Boulder (N/A)	2a, 3a, 3b, 3c, 3d
<i>Station L21</i>	-77.0552	142.6220	-4686	Isop	Boulder (N/A)	6a, 6c, 6d
<i>Station L22</i>	-77.1993	142.6219	-4688	Isop	Regolith/Boulder (N/A)	6a, 6c, 6d, (7b, 7c)
<i>Station L23</i>	-77.2073	142.5837	-4685	lsc/Isop	Boulder (N/A)	6a, 6c, 6d
<i>Station L24</i>	-77.3054	142.8158	-4680	lsc	Boulder (N/A)	6a, 6c, 6d
<i>Station L25</i>	-77.3787	142.5967	-4615	lsc	Regolith (2000)	1a, 1b, 1c, 1e, 6a, 6c, 6d, 7b, 7c
<i>Station L26</i>	-77.4581	142.0336	-4599	lsc/Isop	Boulder (N/A)	6a, 6c, 6d
Landing site 2	-77.4732	141.8233	-4597		(Total: 10.0 kg)	
<i>Station L27</i>	-77.5210	142.1097	-4630	Isop	Boulder (N/A)	6a, 6c, 6d
<i>Station L28</i>	-77.6336	142.0954	-4622	Isop	Boulder (N/A)	6a, 6c, 6d
<i>Station L29</i>	-77.6596	142.0155	-4609	Isop/lsc	Boulder (N/A)	6a, 6c, 6d
<i>Station L30</i>	-77.7209	142.4214	-4628	Isop	Mixed Rake (1000)	1a, 1b, 1c, 1e, 6a, 6c, 6d
<i>Station L31</i>	-77.8093	142.1883	-4605	Isop/lsc	Boulder (N/A)	6a, 6c, 6d
<i>Station L32</i>	-77.8770	142.2026	-4609	lsc/Isop	Boulder (N/A)	6a, 6c, 6d
<i>Station L33</i>	-78.0937	142.0777	-4608	Ish	Boulder (N/A)	6a, 6c, 6d
<i>Station L34</i>	-78.0927	142.0508	-4609	Ish	Boulder (N/A)	6a, 6c, 6d
<i>Station L35</i>	-78.0954	142.0484	-4607	Ish	Regolith (N/A)	7b, 7c
<i>Station L36</i>	-78.1133	141.6494	-4571	Ish	Boulder (N/A)	6a, 6c, 6d
<i>Station L37</i>	-78.3246	142.5125	-4617	lsc	Boulder (N/A)	6a, 6c, 6d
<i>Station L38</i>	-78.4942	142.3218	-4615	Ish/lw/lsc	Boulder (N/A)	2a, 3a, 3b, 3c, 3d, 6a, 6c, 6d
<i>Station L39</i>	-78.5627	141.5129	-4521	lw/Ish	Boulder (N/A)	2a, 3a, 3b, 3c, 3d, 6a, 6c, 6d
<i>Station L40</i>	-78.5974	141.1479	-4489	lw/Ish	Boulder (N/A)	2a, 3a, 3b, 3c, 3d, 6a, 6c, 6d
<i>Station L41</i>	-78.6726	141.0683	-4375	lw/Ish	Boulder (N/A)	2a, 3a, 3b, 3c, 3d, 6a, 6c, 6d

Station L42	-78.7209	140.8983	-4309	lw	Boulder (N/A)	2a, 3a, 3b, 3c, 3d
Station L43 ^d	-78.9803	139.8941	-4164	lw	Mixed Rake (1000)	1a, 1b, 1c, 1e, 2a, 3a, 3b, 3c, 3d, 6a, 6c, 6d
Station L44 ^d	-79.1208	140.0125	-3548	lw	Boulder (5000) ^b	1a, 1b, 1c, 1e, 2a, 3a, 3b, 3c, 3d
ALT: Station L45 ^e	-79.1203	139.0837	-3607	lw	Mixed Rake (1000)	1a, 1b, 1c, 1e, 2a, 3a, 3b, 3c, 3d
ALT: Station L46 ^e	-79.1515	139.0631	-3224	lw	Boulder (5000) ^b	1a, 1b, 1c, 1e, 2a, 3a, 3b, 3c, 3d
ALT: Station L47 ^e	-78.1885	139.0997	-2736	lw	Mixed Rake (1000)	1a, 1b, 1c, 1e, 2a, 3a, 3b, 3c, 3d
Station L48 ^d	-78.9845	139.5554	-4177	lw/lsh	Mixed Rake (1000)	1a, 1b, 1c, 1e, 2a, 3a, 3b, 3c, 3d, 6a, 6c, 6d
Station L49	-78.9254	139.6857	-4220	lw	Boulder (N/A)	2a, 3a, 3b, 3c, 3d, 6a, 6c, 6d
Station L50	-78.8769	139.6190	-4318	lsh	Boulder (N/A)	2a, 3a, 3b, 3c, 3d
Station L51	-78.6734	139.5241	-4311	lsh	Regolith (2000)	1a, 1b, 1c, 6a, 6d, 7b, 7c
Landing Site 3	-78.6619	139.5242	-4314		(Total: 10 kg)	
					(Traverse total: 29.5 kg)	

^aBased on M3 spectra considered to be a crystalline, homogeneous rock (sample mass after Shearer et al., 2007)

^bAssumed to be heterogeneous impact melt breccia (sample mass after CAPTEM, 2007)

¹Kramer et al. (2013) ²Based on CAPTEM recommendations (Shearer et al., 2007) ³NRC (2007) ⁴Proposed sites from this study to sample SPA material ⁵Alternative sites for sampling SPA material based on Hurwitz and Kring (2015)

Table S.3. The collected lithologies and their relative abundances during each section of the short and long traverse based on CAPTEM recommendations (Shearer et al., 2007).

	Basalt	Impact breccia	Regolith	Homogeneous ^a
Short traverse				
Section 1	0.0	0.6	0.2	0.2
Section 2	0.1	0.5	0.4	0.0
Section 3	0.1	0.7	0.2	0.0
Long traverse				
Section 1	0.0	0.6	0.2	0.2
Section 2	0.0	0.7	0.2	0.1
Section 3	0.0	0.8	0.2	0.0

^aHomogeneous rocks include anorthosites, norites and dunites.

Table S.4. Properties of each engine type.

	Aestus	Aestus II	AJ-10	R-40B
Propellant type	MMH	MMH	Aerozine 50	MMH
Oxidizer	NTO	NTO	NTO	NTO
Propellant boiling point (F)	190	190	158	190
Propellant freezing point (F)	-62.3	-62.3	19.4	-62.3
ISP (s)	324	340	319	293
Thrust (N)	29600	55400	43700	4000
Dry mass (kg)	111 kg	138 kg	100 kg	6.8 kg

Table S.5. Boulder locations and properties that were used to assess the bearing capacity of the pyroclastic material.

Boulder	Latitude	Longitude	Boulder Radius (cm)	Radius at Surface (cm)	Track Width (m)	Track Length (m)	Slope (°)	Track Depth (cm)
1	-75.156	140.118	297.5	275	4.14	120	2-4	183
2	-75.163	140.131	259	251	3.68	98	2-4	195
3	-75.309	139.173	544.5	521	6.5	356	10-12	387

Table S.6. Calculations of the bearing capacity (dynes/cm²) of the pyroclastic material for an assumed internal friction angle of 30°.

Boulder	Soil Density = 2 g/cm ²		Soil Density = 2.29 g/cm ²	
	Bearing Capacity (dynes/cm ²)	Bearing Capacity (kN/m ²)	Bearing Capacity (dynes/cm ²)	Bearing Capacity (kN/m ²)
1	2.60 x 10 ⁶	2.57 x 10 ⁵	2.80 x 10 ⁶	2.80 x 10 ⁵
2	2.59 x 10 ⁶	2.59 x 10 ⁵	2.81 x 10 ⁶	2.81 x 10 ⁵
3	5.19 x 10 ⁶	5.19 x 10 ⁵	5.62 x 10 ⁶	5.62 x 10 ⁵
Average	3.46 x 10 ⁶	3.45 x 10 ⁵	3.74 x 10 ⁶	3.74 x 10 ⁵

Table S.7. Calculations of the bearing capacity (dynes/cm²) of the pyroclastic material for an assumed internal friction angle of 35°.

Boulder	Soil Density = 2 g/cm ²		Soil Density = 2.29 g/cm ²	
	Bearing Capacity (dynes/cm ²)	Bearing Capacity (kN/m ²)	Bearing Capacity (dynes/cm ²)	Bearing Capacity (kN/m ²)
1	4.82 x 10 ⁶	4.82 x 10 ⁵	5.18 x 10 ⁶	5.18 x 10 ⁵
2	4.79 x 10 ⁶	4.79 x 10 ⁵	5.17 x 10 ⁶	5.17 x 10 ⁵
3	9.62 x 10 ⁶	9.62 x 10 ⁵	1.04 x 10 ⁷	1.04 x 10 ⁶
Average	6.41 x 10 ⁶	6.41 x 10 ⁵	6.91 x 10 ⁶	6.91 x 10 ⁵

Table S.8. Summary of trade study between KA-band and laser communication.

	KA-band	Laser
Data rate	5-100 Mbps	Up to 600 Mbps
Bandwidth	32 GHz	300,000 GHz
Power		Half of KA-band
Heritage	>15 missions	LLCD
Earth weather impact	No	Yes
No. of ground stations required	Currently >4, sufficient	Additional needed
Forward application for Mars	No, currently in use	Yes
Download time for "Apollo 13" movie (36,000 MB)	49.1 minutes	7.9 minutes

Fig. S.1. The mass capability for different sample container internal diameters assuming the lithology sample proportions from Table S.1. The minimum and maximum mass capabilities were calculated using the upper and lower bound of the estimated densities of each lithology (see text).

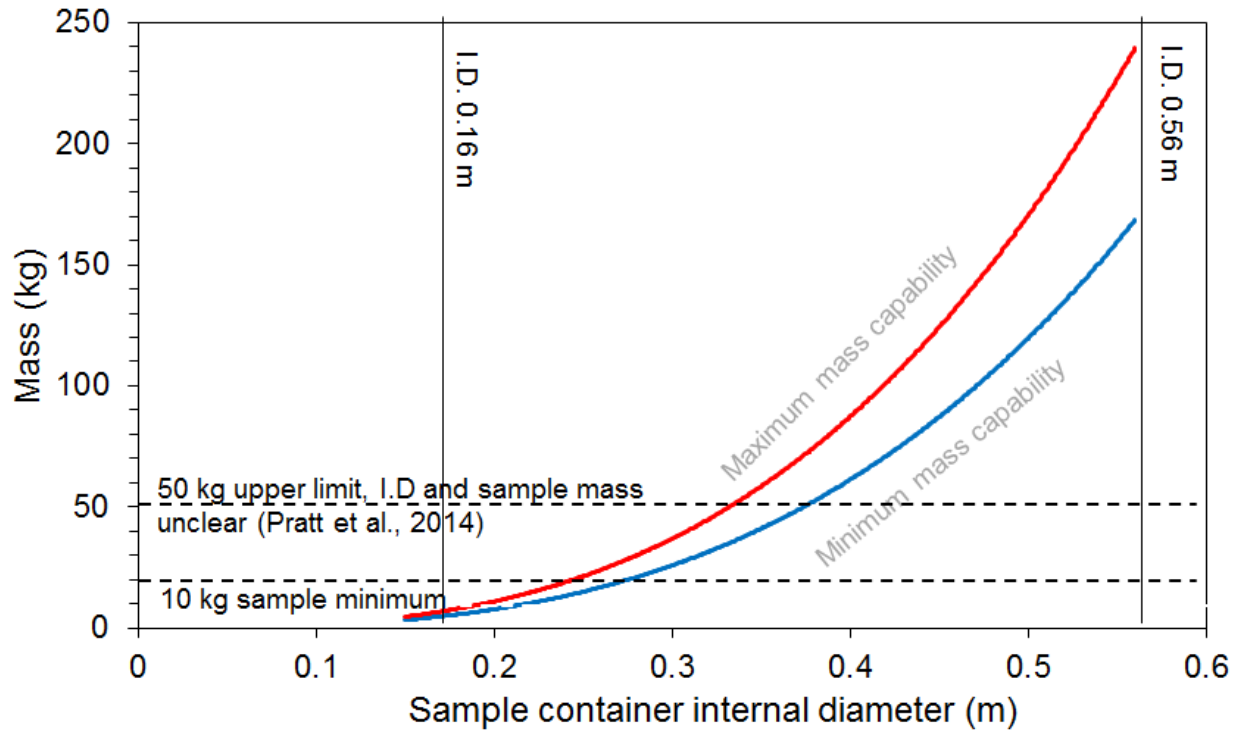


Fig. S.2. The maximum payload (kg) as a function of the ascent vehicle tanksize volume (m^3).

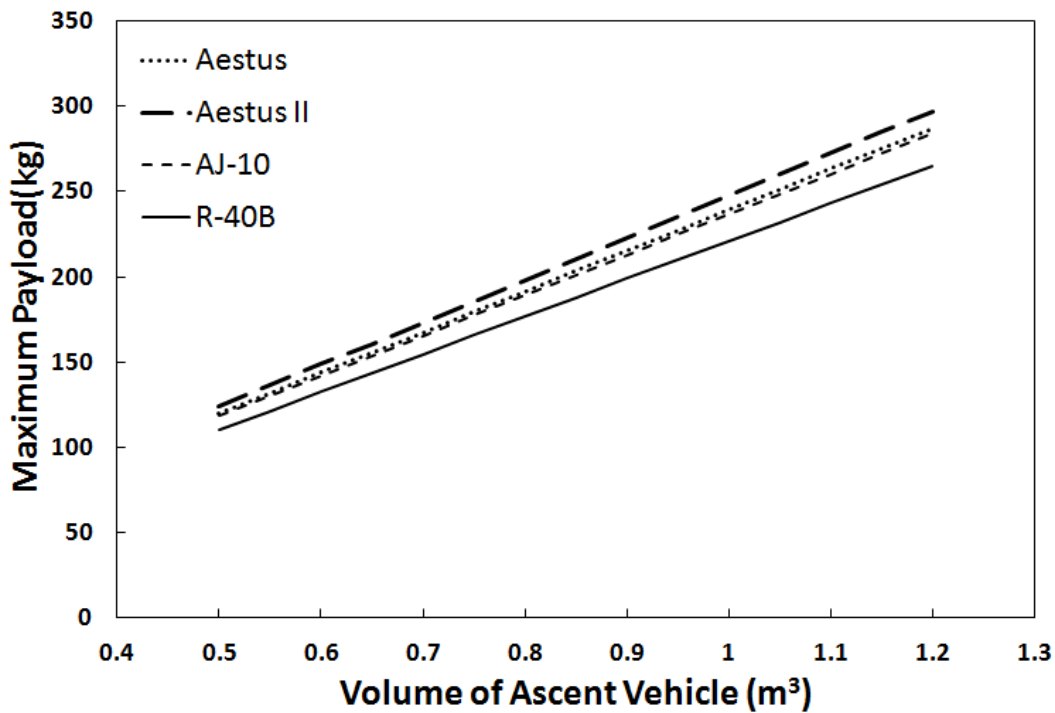


Fig. S.3. Dimensions of the ascent vehicle as a function of payload size (sample mass) assuming an Aestus II engine with Monomethylhydrazine (MMH) propellant. The left-most vehicle represents the size of the vehicle required for the 11 kg payload, and the others explore what would be required to deliver larger payloads from the lunar surface to the eDSH (20, 50 and 100 kg, respectively).

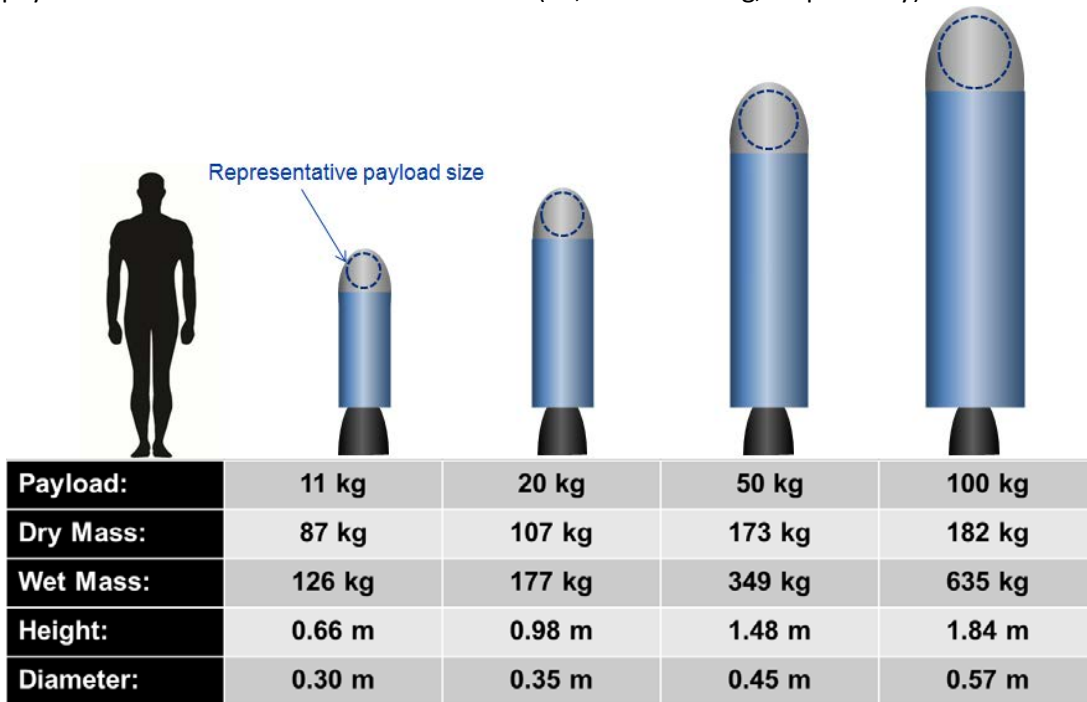


Fig. S.4. Qualitative assessment of crater degradation state of craters along the short and long traverse (modified from Wilhelms, 1984)

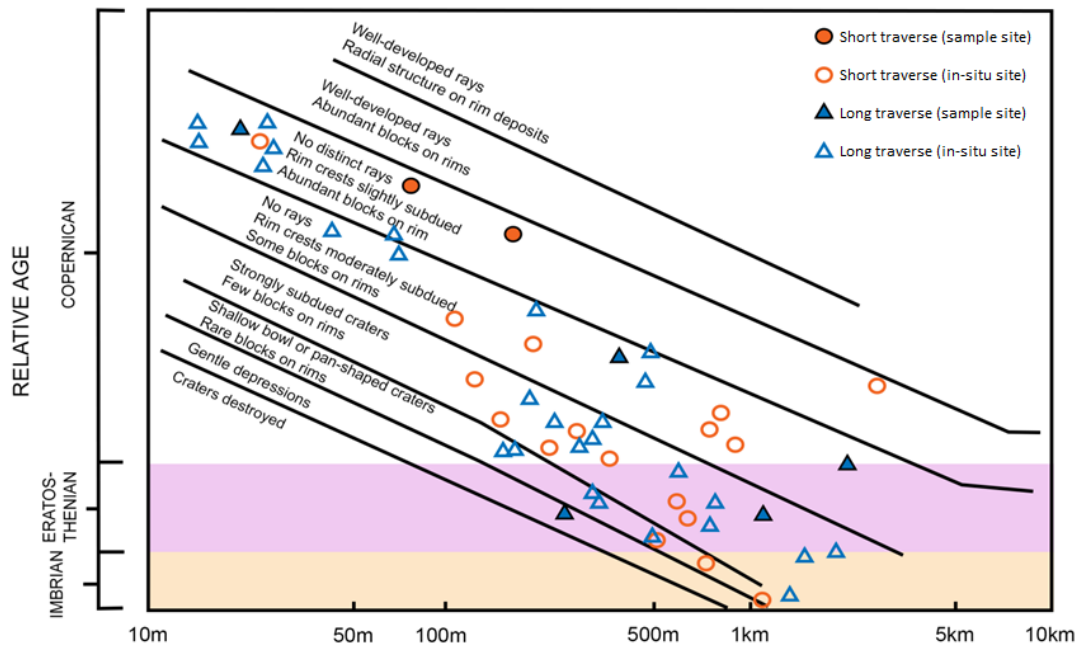


Figure 1A-B

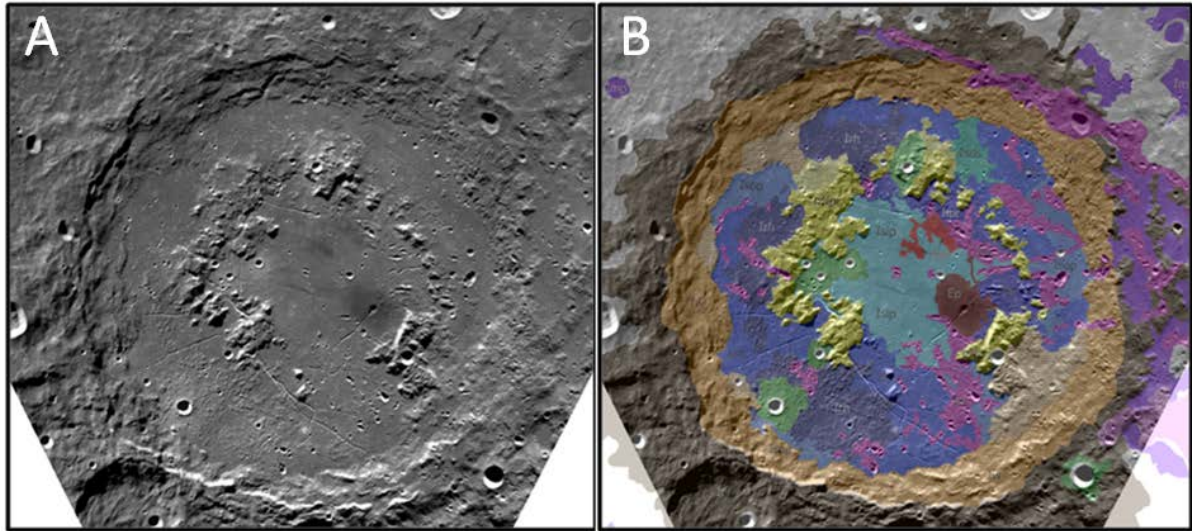


Figure 2

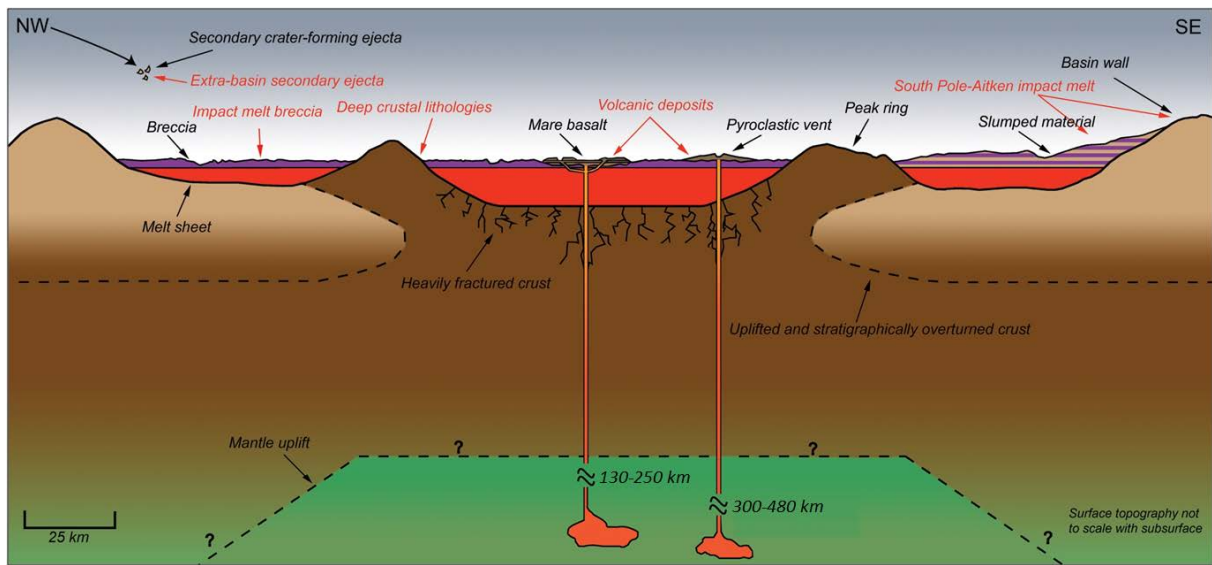


Figure 3

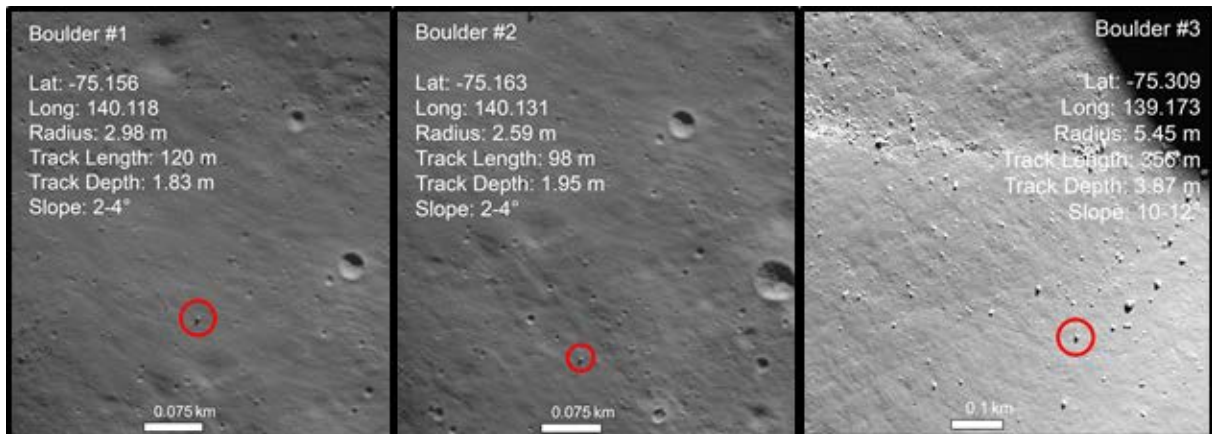
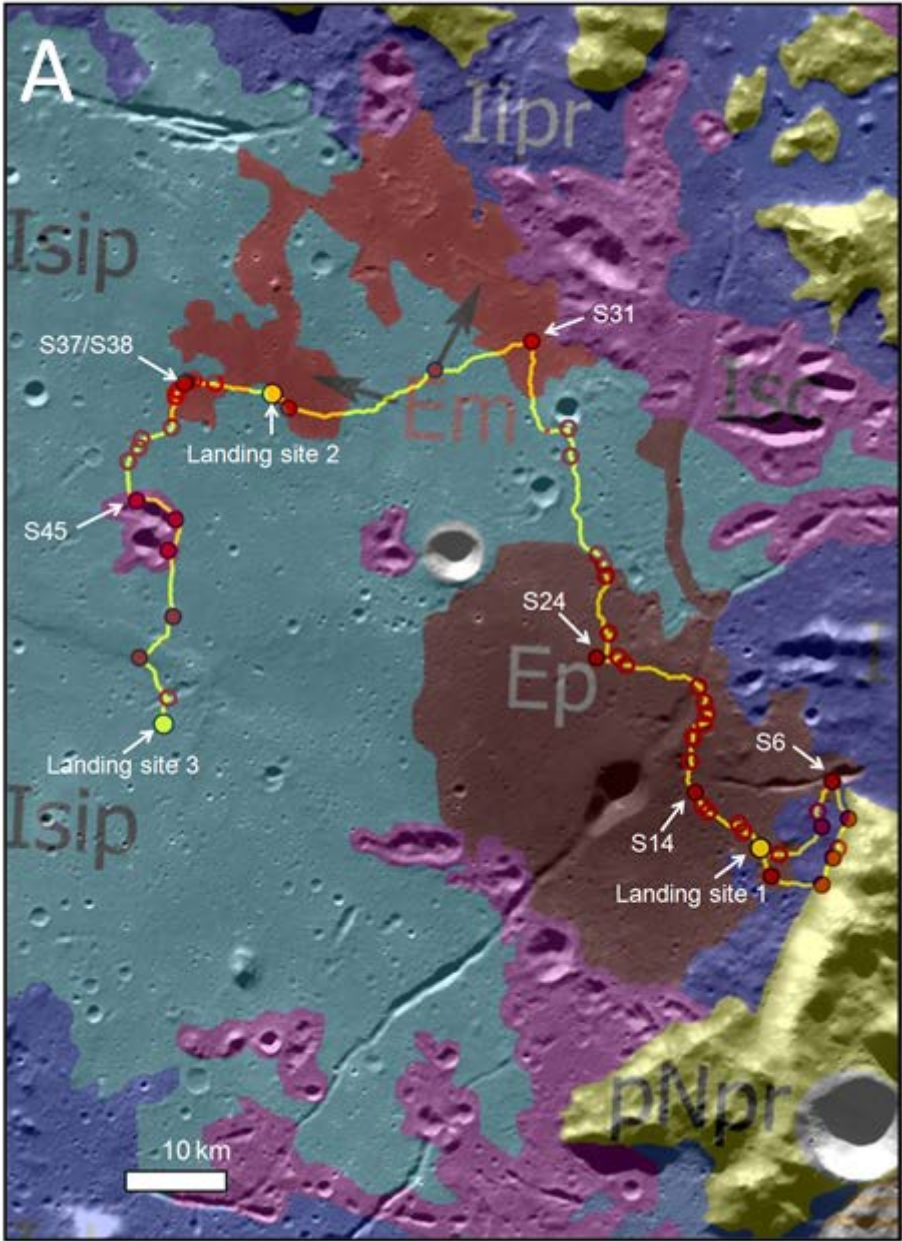


Figure 4A-B



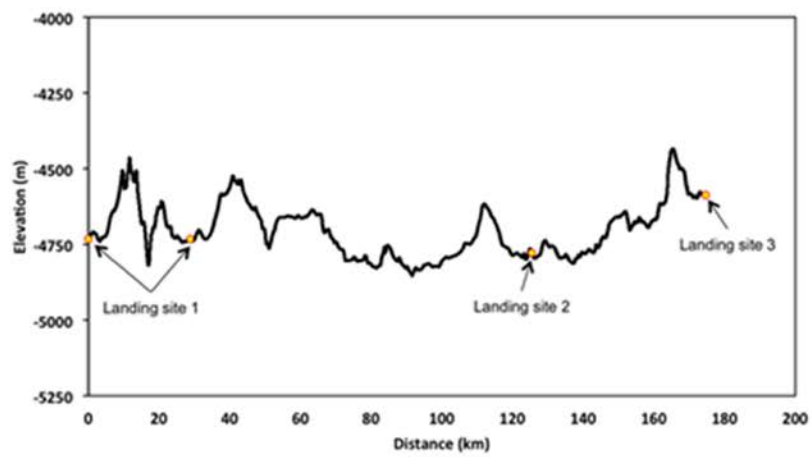
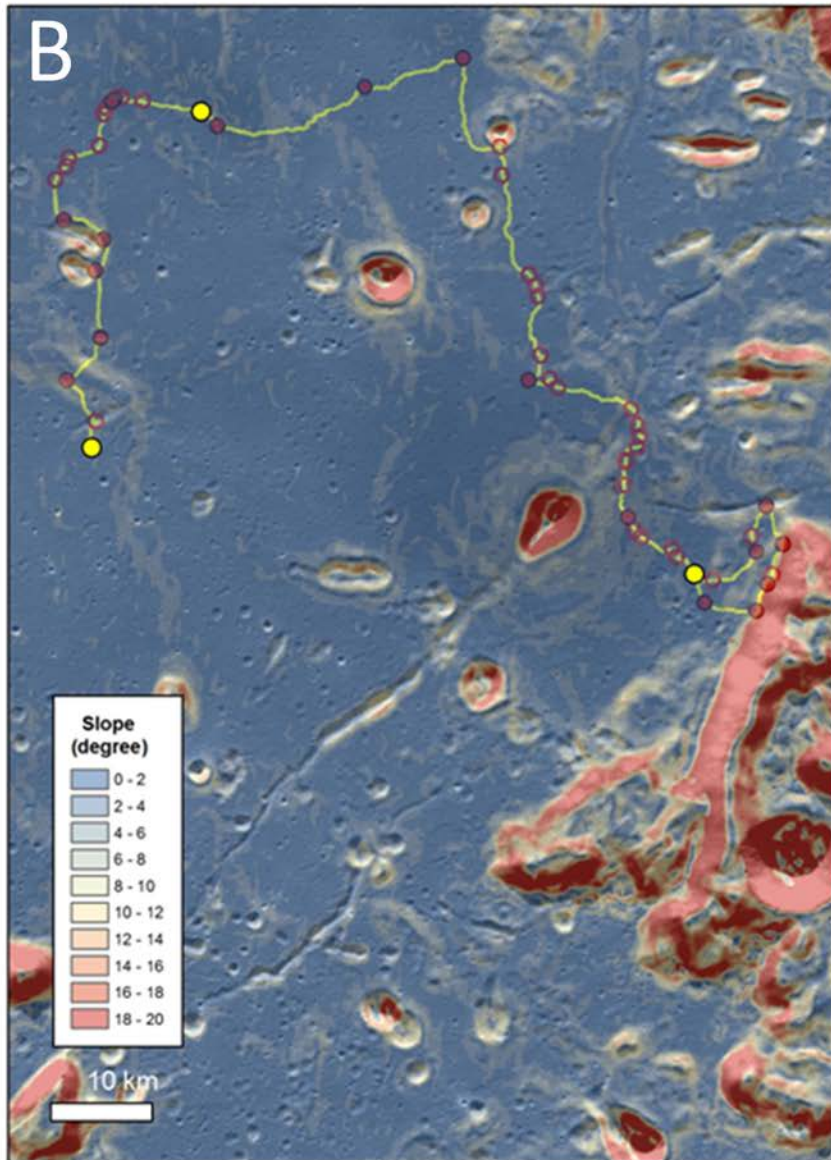


Figure 5A-E

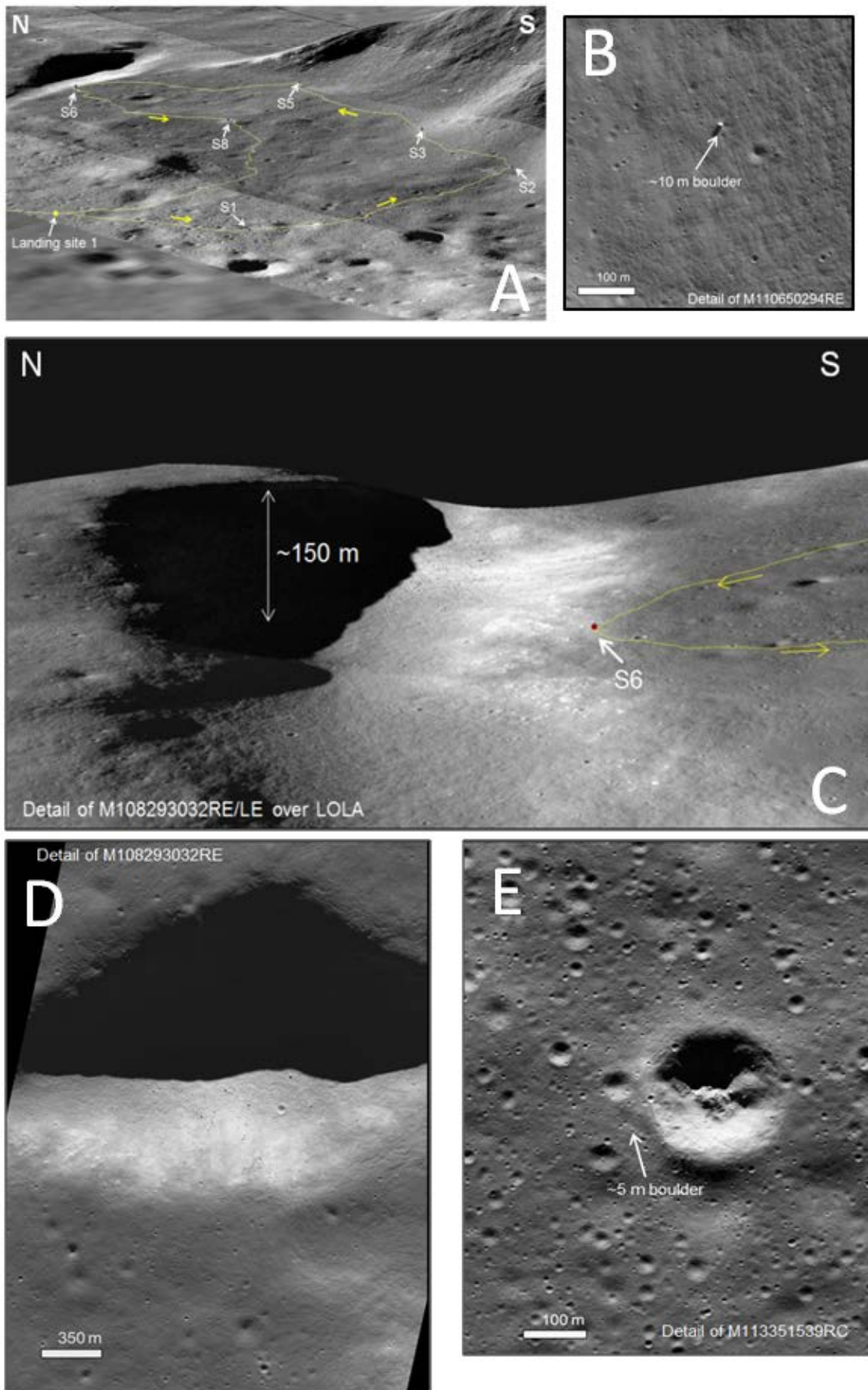


Figure 6

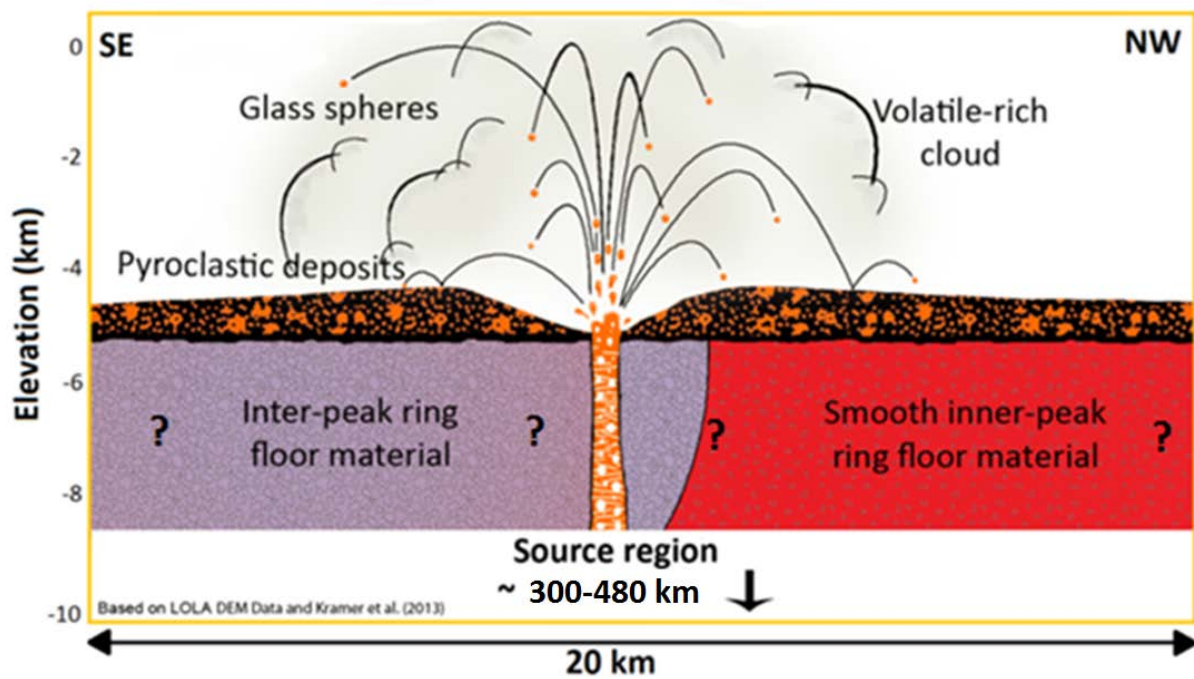


Figure 7

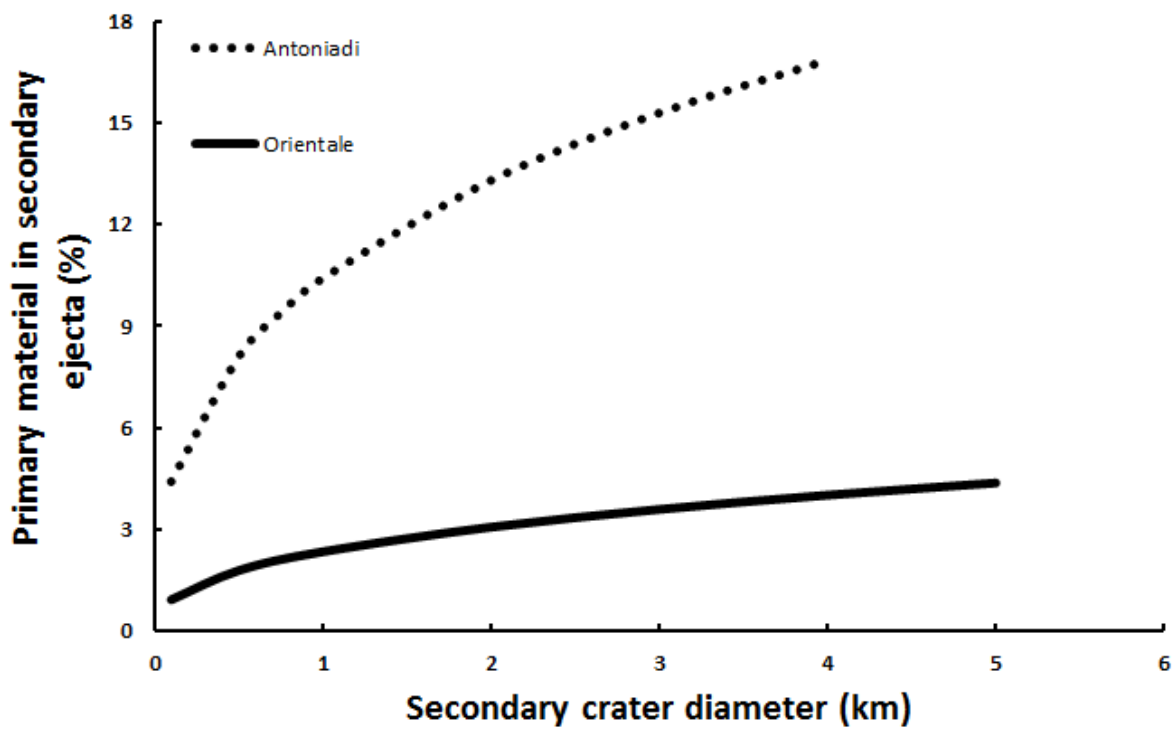
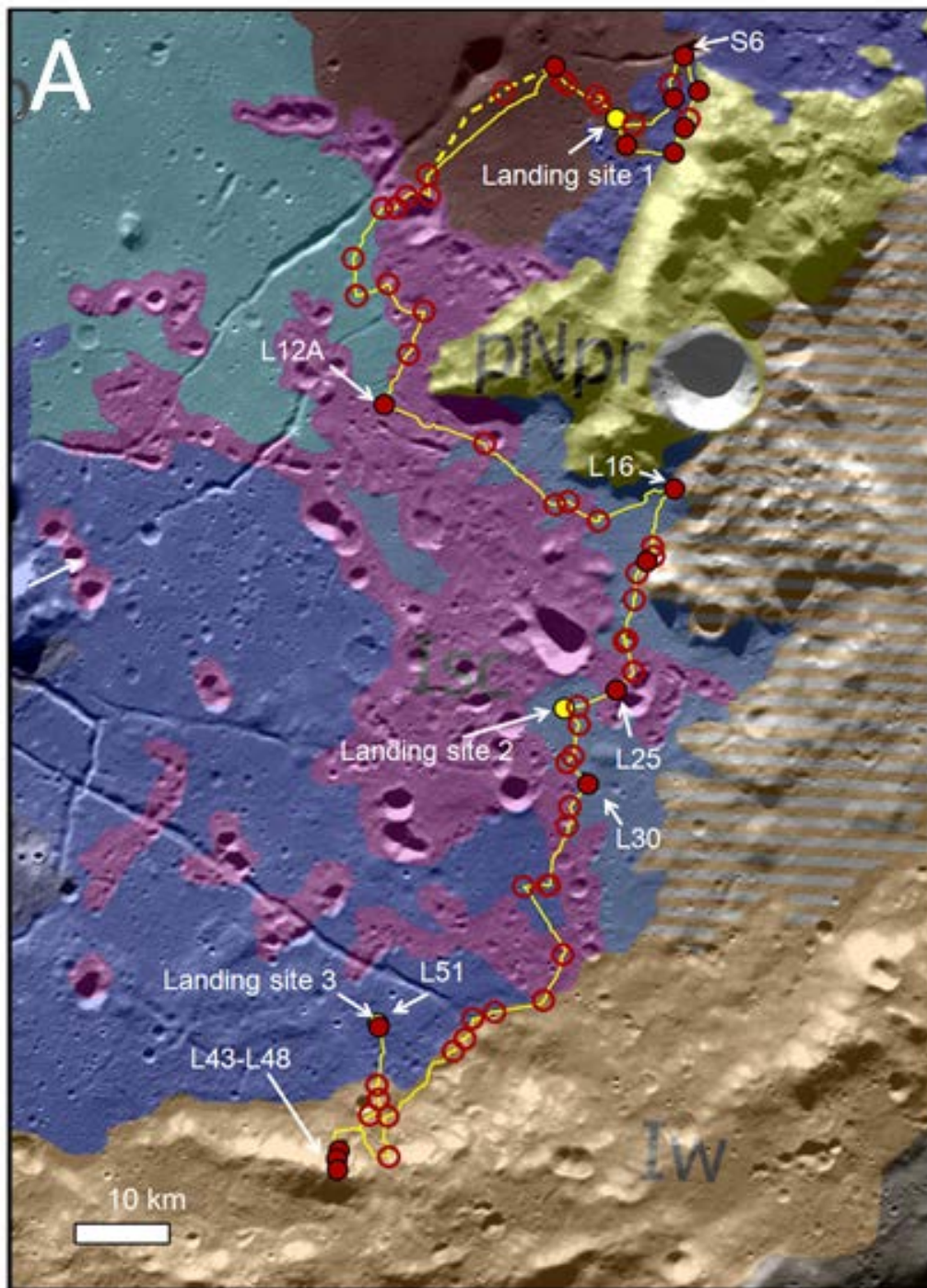


Figure 8A-B



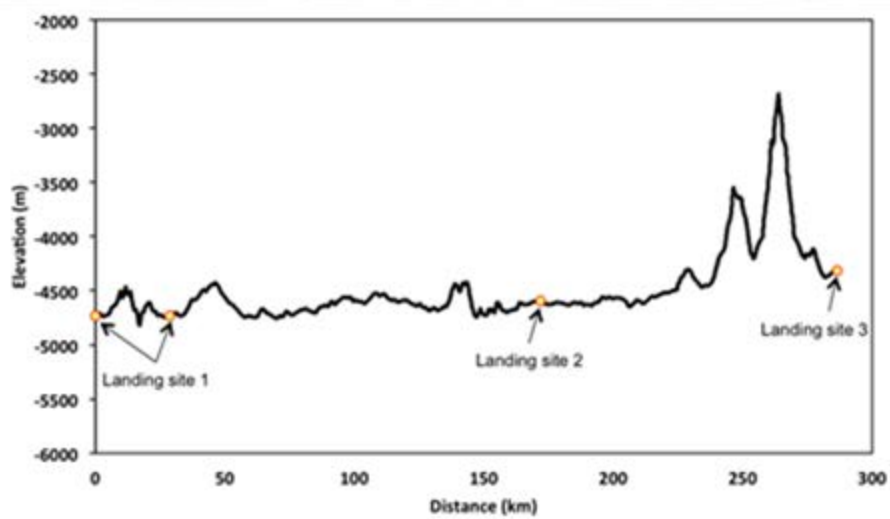
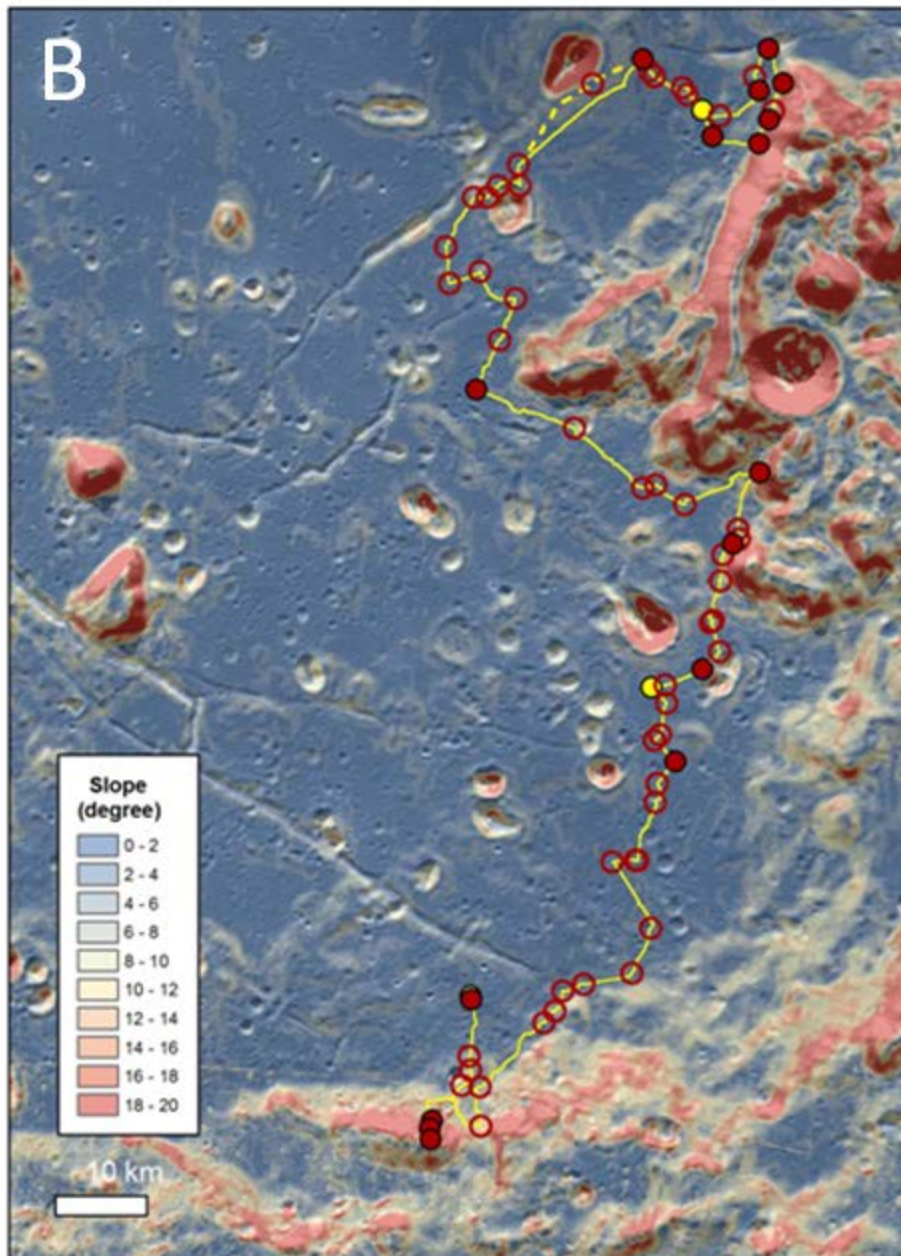


Figure 9A-G

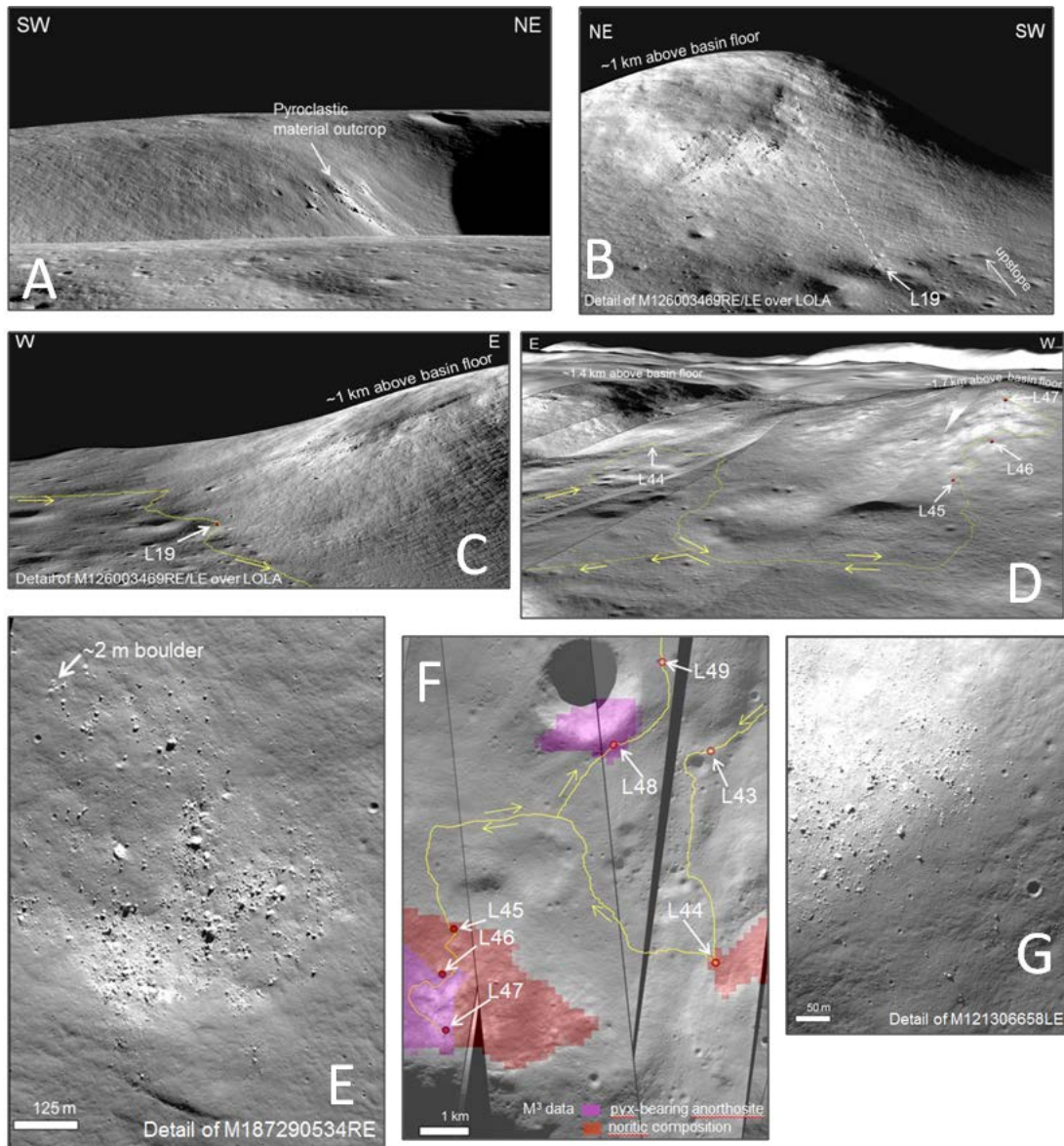


Table 1 Notional instrumentation suite assumed for ConOps assessment.

Instrument	Dimensions (cm)	Weight (kg)^a	Power (W)^a	Data rate (kbps)
Ground penetrating radar (ExoMars WISDOM) ^[1]	Sensor: 10x10x1 Electronics: 10x6x6	<3.50	<7.8	44.5
Arm-mounted Alpha Particle X-Ray spectrometer (MER) ^[2]	10.5x6x9	<2.20	<7.3	18.0**
Gamma Ray spectrometer (JH APL) ^[3]	Sensor: 8x8x8 DPU: 10x15x5	<1.82	<3.25	0.01-0.1
Neutron spectrometer (Lunar Prospector/HYDRA) ^[1]	18x12x6	<0.65	<1.8	0.5
Microscope camera (MER) ^[2]	8x8x10	<0.4	<0.4	8000 ^b
Surface imaging camera (MSL MastCam) ^[1]	11x29x12	<1.0	<11.0	1.26

^aWith 30% contingency^bDefined as science data rate prior to on-board processing

References: [1] Shearer et al. (2010) [2] Arvidson and May (2010) [3] Wieczorek et al. (2015)

Table 2 ConOps used for traverse times assuming the notional instrumental payload from Table 1.

Station Activities	Time (Earth hours)^a
Panoramic image using 3D imager (HD video feed at other times) ^[1]	8
Position rover for in-situ target ^[1]	0.5
GPR analysis ^[2]	On while traversing
Neutron sensor analysis ^[2]	On as when needed including during traversing
Position arm-mounted APXS ^[1]	0.5
APXS analysis ^[4]	3.0
Position GRS ^[1]	0.5
GRS analysis ^[3]	1.0
Position microscope camera (LRAC) ^[1]	0.5
Microscope camera (LRAC) ^[4]	1.0
Surface imager (MSL MastCam) ^[2]	0.5
Sample collection ^{[1]b}	3.0
Sample transfer to bag and storage ^[1]	1.0

^aAssuming one analysis per type of in-situ analysis^bSample collection may vary considerably dependent on collection method (e.g., scoop, rake, drilling)

References: [1] Potts et al. (2015) [2] Shearer et al. (2010) [3] Wieczorek et al. (2015) [4] Arvidson and May (2010) [5] Malin et al. (2005)

Table 3 Summary of the NRC (2007) science goals that can be addressed within the short (a) and long traverse (b). Goals that with reasonable certainty can be addressed within the traverse are indicated in dark grey, goals that may be addressed are indicated in light grey and the top 10 of the highest science priorities are in italic and bold.

a

	a	b	c	D	e
1: Bombardment history of the inner solar system	<i>Test cataclysm hypothesis</i>	<i>Early Earth-Moon impact flux and age of SPA basin</i>	<i>Establish absolute chronology</i>	Recent impact flux	Role of secondary craters on crater counts
2: Structure and composition of the lunar interior	<i>Thickness and lateral variability of lunar crust</i>	<i>Chemical and physical stratification of lunar mantle</i>	<i>Size, composition and physical state of lunar core</i>	Thermal state and evolution of lunar interior	
3: Diversity of lunar crustal rocks	<i>Extent and composition of differentiation products</i>	<i>Age, distribution and origin of lunar rock types</i>	Composition of lower crust and bulk Moon	Local and regional complexity of lunar crust	Extent and structure of megaregolith
4: Lunar poles and volatiles	<i>Compositional state and distribution of volatiles</i>	Source(s) for lunar polar volatiles	Dynamical processes of polar volatiles	Physical properties of cold polar regolith	Polar regolith and ancient solar environment
5: Lunar volcanism	Origin and variability of basalts	Age of youngest and oldest mare basalts	Compositional range and extent of pyroclastics	Flux and evolution of lunar volcanism	
6: Impact processes	Existence and extent of melt sheet differentiation	Structure of multi-ring impact basins	Physical aspects of crater formation	Lateral and vertical mixing of ejecta and local material	
7: Regolith processes	Characterizing ancient regolith	Physical properties of regolith	Regolith modification processes	Studying rare materials in regolith	

b

	a	b	c	d	e
1: Bombardment history of the inner solar system	<i>Test cataclysm hypothesis</i>	<i>Early Earth-Moon impact flux and age of SPA basin</i>	<i>Establish absolute chronology</i>	Recent impact flux	Role of secondary craters on crater counts
2: Structure and composition of the lunar interior	<i>Thickness and lateral variability of lunar crust</i>	<i>Chemical and physical stratification of lunar mantle</i>	<i>Size, composition and physical state of lunar core</i>	Thermal state and evolution of lunar interior	
3: Diversity of lunar crustal rocks	<i>Extent and composition of differentiation products</i>	<i>Age, distribution and origin of lunar rock types</i>	Composition of lower crust and bulk Moon	Local and regional complexity of lunar crust	Extent and structure of megaregolith
4: Lunar poles and volatiles	<i>Compositional state and distribution of volatiles</i>	Source(s) for lunar polar volatiles	Dynamical processes of polar volatiles	Physical properties of cold polar regolith	Polar regolith and ancient solar environment
5: Lunar volcanism	Origin and variability of basalts	Age of youngest and oldest mare basalts	Compositional range and extent of pyroclastics	Flux and evolution of lunar volcanism	
6: Impact processes	Existence and extent of melt sheet differentiation	Structure of multi-ring impact basins	Physical aspects of crater formation	Lateral and vertical mixing of ejecta and local material	
7: Regolith processes	Characterizing ancient regolith	Physical properties of regolith	Regolith modification processes	Studying rare materials in regolith	

